NAVAL POSTGRADUATE SCHOOL

MONTEREY, CALIFORNIA

THESIS

BORON-NITRIDE NANOTUBES AND VERSATILE DIELECTRICS FOR MEMS ELECTRONIC NOSE RADIATION DETECTOR

by

Zishan Hameed and John V. Gats

June 2019

Thesis Advisor: Dragoslav Grbovic
Co-Advisor: Craig F. Smith

THIS PAGE INTENTIONALLY LEFT BLANK

REPORT DOCUMENTATION PAGE			*Form Approved OMB No. 0704-0188*

1. AGENCY USE ONLY *(Leave blank)*	**2. REPORT DATE** June 2019	**3. REPORT TYPE AND DATES COVERED** Master's thesis

4. TITLE AND SUBTITLE
BORON-NITRIDE NANOTUBES AND VERSATILE DIELECTRICS FOR MEMS ELECTRONIC NOSE RADIATION DETECTOR

5. FUNDING NUMBERS

6. AUTHOR(S) Zishan Hameed and John V. Gats

7. PERFORMING ORGANIZATION NAME(S) AND ADDRESS(ES)
Naval Postgraduate School
Monterey, CA 93943-5000

8. PERFORMING ORGANIZATION REPORT NUMBER

9. SPONSORING / MONITORING AGENCY NAME(S) AND ADDRESS(ES)
N/A

10. SPONSORING / MONITORING AGENCY REPORT NUMBER

11. SUPPLEMENTARY NOTES The views expressed in this thesis are those of the author and do not reflect the official policy or position of the Department of Defense or the U.S. Government.

12a. DISTRIBUTION / AVAILABILITY STATEMENT
Approved for public release. Distribution is unlimited.

12b. DISTRIBUTION CODE
A

13. ABSTRACT (maximum 200 words)

As society's use of radiation-producing technologies increases, so does the need to create more effective and versatile radiation detectors. Low-cost, low-power, compact radiation detectors are applicable across an ever-growing range of fields and industries. Micro-electro-mechanical systems (MEMS) and other printed fabrication technology can enable future mass production of versatile radiation sensors while maintaining reliability and low costs. By utilizing the electronic nose framework, combining an array of sensors to low-cost computing, we propose a new method of robust real-time radiation detection. This thesis explores both the fabrication process of MEMS sensors and the testing of various new materials designed to respond to gamma and neutron irradiation. Through three iterations of sensor creation at Naval Postgraduate School and NASA, and subsequent testing of those sensors, a sensor combining carbon nanotubes and boron-nitride nanotubes successfully registered thermal neutron irradiation. A different sensor, combining MEMS capacitors with varying dielectric materials, did not register gamma irradiation during testing. The neutron detection results simply confirmed the presence of neutron irradiation. We recommend future testing to measure specific response to energy and fluence of neutrons, to redesign the MEMS chip and to change the dielectric detection materials.

14. SUBJECT TERMS
MEMS, radiation, radiation detection, dielectric, boron-nitride, nanotube, nose

15. NUMBER OF PAGES
93

16. PRICE CODE

17. SECURITY CLASSIFICATION OF REPORT	**18. SECURITY CLASSIFICATION OF THIS PAGE**	**19. SECURITY CLASSIFICATION OF ABSTRACT**	**20. LIMITATION OF ABSTRACT**
Unclassified	Unclassified	Unclassified	UU

NSN 7540-01-280-5500

Standard Form 298 (Rev. 2-89)
Prescribed by ANSI Std. 239-18

THIS PAGE INTENTIONALLY LEFT BLANK

Approved for public release. Distribution is unlimited.

BORON-NITRIDE NANOTUBES AND VERSATILE DIELECTRICS FOR MEMS ELECTRONIC NOSE RADIATION DETECTOR

Zishan Hameed
Lieutenant, United States Navy
BS, U.S. Naval Academy, 2011

John V. Gats
Captain, United States Marine Corps
BS, Gonzaga University, 2012

Submitted in partial fulfillment of the
requirements for the degree of

MASTER OF SCIENCE IN APPLIED PHYSICS

from the

NAVAL POSTGRADUATE SCHOOL
June 2019

Approved by: Dragoslav Grbovic
Advisor

Craig F. Smith
Co-Advisor

Kevin B. Smith
Chair, Department of Physics

THIS PAGE INTENTIONALLY LEFT BLANK

ABSTRACT

As society's use of radiation-producing technologies increases, so does the need to create more effective and versatile radiation detectors. Low-cost, low-power, compact radiation detectors are applicable across an ever-growing range of fields and industries. Micro-electro-mechanical systems (MEMS) and other printed fabrication technology can enable future mass production of versatile radiation sensors while maintaining reliability and low costs. By utilizing the electronic nose framework, combining an array of sensors to low-cost computing, we propose a new method of robust real-time radiation detection. This thesis explores both the fabrication process of MEMS sensors and the testing of various new materials designed to respond to gamma and neutron irradiation. Through three iterations of sensor creation at Naval Postgraduate School and NASA, and subsequent testing of those sensors, a sensor combining carbon nanotubes and boron-nitride nanotubes successfully registered thermal neutron irradiation. A different sensor, combining MEMS capacitors with varying dielectric materials, did not register gamma irradiation during testing. The neutron detection results simply confirmed the presence of neutron irradiation. We recommend future testing to measure specific response to energy and fluence of neutrons, to redesign the MEMS chip and to change the dielectric detection materials.

THIS PAGE INTENTIONALLY LEFT BLANK

TABLE OF CONTENTS

LIST OF FIGURES

THIS PAGE INTENTIONALLY LEFT BLANK

LIST OF TABLES

THIS PAGE INTENTIONALLY LEFT BLANK

LIST OF ACRONYMS AND ABBREVIATIONS

Al	aluminum
BNNT	boron nitride nanotube
C-C	carbon-carbon
CNT	carbon nanotube
DHS	Department of Homeland Security
DSN	distributed sensor network
DT	deuterium-tritium
IR	infrared
LLNL	Lawrence Livermore National Laboratory
MEMS	micro-electro-mechanical systems
PDMS	polydimethylsiloxane
PuBe	plutonium-beryllium
PVA	polyvinyl alcohol
SEM	scanning electron microscope
Si	silicon
SiO_2	silicon dioxide
SOI	silicon on insulator
SWCNT	single walled carbon nanotube
TLD	thermoluminescence dosimeter
Z	atomic number

THIS PAGE INTENTIONALLY LEFT BLANK

ACKNOWLEDGMENTS

We would first like to express our gratitude to the faculty at NPS, namely our advisors Dr. Grbovic and Dr. Smith. Their trust in us to accomplish the task and support for our ideas along the way were greatly appreciated. As the experiments continued, their guidance and hands-on assistance was invaluable to the project's success. We also owe Dr. Luhrs in the Mechanical and Aerospace Engineering Department a huge debt of gratitude for her selfless and comprehensive assistance. This project surely would not have succeeded without her. Finally, Dr. Lee in the Physics Department went above and beyond anything we could have expected in his structuring of circuits and guidance in experimental set up at multiple stages in the testing.

Outside of NPS, we have to thank our collaborators at NASA and Lawrence Livermore National Laboratory (LLNL) for their enthusiastic and expert work in support of the project. At NASA's Ames Research Center, Dr. Han, Dr. Meyyappan, and their team made the sensor a reality with their expertise in material science and experimental methods. Dr. Kerr at LLNL spent multiple days working with us in his lab, where his knowledge and experience facilitated what became a successful test.

THIS PAGE INTENTIONALLY LEFT BLANK

I. INTRODUCTION

As society's use of radiation-producing technologies has increased, so has the need to create more powerful and effective detectors. Radiation detection, as both a scientific and an engineering endeavor, began in the 1890s and has evolved throughout the last century into a diverse field with many applications [1]. As the knowledge and capabilities surrounding radiation and its classification have increased, detectors have grown from the ability to merely detect the presence of radiation, to the ability to categorize and quantify it. In 2017, the global radiation detection, monitoring, and safety market was valued at $1.71 billion. In 2022, that market is projected to be at $2.26 billion. That growth projection is driven by security concerns, expansion of radiation use in medicine, and increased cognizance of individuals working in environments with radiation exposure [2].

The style of radiation detector discussed in this thesis will operate similarly to a nose, and be effective across wide-ranging areas of application. An electronic nose was first introduced in 1982 [3] and works similarly to the mammalian olfactory system. The human nose is capable of discriminating upward of 10,000 smells using only about 400 receptors [4]. The nose works together with the brain to accomplish this by breaking down smells into specific elements, which are detected in the nose and subsequently quantified by olfactory sensory neurons in the brain. The neurons send this information to the brain, where the signals are recombined and identified by tapping into one's memory and experience [5]. According to Wilson and Baietto in [6], much like the human olfactory system, "an electronic nose system typically consists of a multisensor array, an information-processing unit such as an artificial neural network, software with digital pattern-recognition algorithms, and reference-library databases." The nose receptors and olfactory sensory neurons are replaced, in this instance, with the multisensor array and the brain in the system is replaced by processing units and algorithms trained to recognize specific sources of radiation through the detection of its constituent parts.

The first mention of an electronic nose specifically for radiation detection was in 2006, when Arshak et al. [7] broadly applied the nose concept to radiation detection. A more modern idea for the materials used for the receptors of the nose originated with Han

et al. [8] at NASA Ames Research Laboratory, who used polydimethylsiloxane (PDMS) as a gate dielectric in a metal oxide semiconductor field effect transistor. This thesis will implement the framework of Arshak et al. [7] and expand on the materials proposed by Han et al. [8] by exploring the responses of two other sensing materials. Those materials, in combination with existing solid-state detector technology, will have the ability to be combined into a multisensor array. The first of the sensors will attempt to make use of a polymer whose dielectric constant is sensitive to gamma radiation. The second of the sensors will employ boron-nitride nanotubes (BNNT) to detect thermal neutron radiation, which ultimately proves successful as a thermal neutron detector.

A. APPLICATIONS FOR THE ELECTRONIC NOSE DETECTOR

Low-cost, low-power, compact, reliable radiation detectors are applicable across many fields, to include homeland security [9], distributed sensor networks (DSN) [10], [11], space operations [12], medicine [13], and dosimetry in connection with health physics [14]. While each of these areas currently boasts its own detection methods, many are task-specific and can be made smaller and less expensively. Utilizing well-established micro-electro-mechanical systems (MEMS) and other printed fabrication methods can enable mass production of versatile radiation sensors while maintaining reliability and low cost.

One area where this technology can be particularly influential is dosimetry in connection with health physics. Currently, personnel in electromagnetic radiation environments commonly use thermoluminescence dosimeter (TLD) badges to quantify their radiation exposure. TLD badges, shown in Figure 1, accumulate radiation damage over time and inform the user (or a health physics professional) of accumulated radiation exposure only after periodic read out.

Figure 1. TLD Badge. Source: [15].

Ideally, a personnel detector could identify radiation exposure in real time while maintaining the low profile currently enjoyed by the TLD. By combining electromagnetic radiation-sensitive materials with low-power computing, the multisensor array could improve this detection technique to enhance radiation detection for personnel.

For neutron detection, gas proportional counters with materials such as boron trifluoride or helium-3 are commonly used; also used are scintillation detectors based on liquid, crystal, glass, or fiber scintillators. In general, detection systems based on these approaches are expensive and bulky. For gas systems, the mechanism of detection is the ionization of an otherwise inert gas, which requires large areas for large detection probabilities [14]. While this apparatus is most suitable for a laboratory, it is much less feasible for deployment on a large scale or for use as an individual operator due to size and cost constraints.

The U.S. Department of Homeland Security (DHS) employs large Radiation Portal Monitors, shown in Figure 2, at seaports across the country as neutron detectors [16]. DHS requires neutron detection at ports of entry because typical fissionable material, such as weapons-grade plutonium, radiates neutrons with a wide spectrum of energies. For a typical nuclear weapon, neutron radiation is unavoidable, so when left unshielded, such a weapon or its fissile core could be detected via its neutron radiation.

Figure 2. Radiation Portal Monitors

Both the Defense Advanced Research Projects Agency [11] and Los Alamos National Laboratory [10] have completed initial investigations into the feasibility of using DSNs for radiation detection. These networks would require the use of new radiation detection techniques that combine smaller sensors with real time detection. The proposed neutron detector component of the multisensor array addresses this issue by leveraging small, lightweight, and relatively inexpensive BNNTs for their ability to detect neutrons. By combining detection techniques and materials, radiation detection for DSNs, personnel protection, and other wide-ranging systems can be enhanced and hardened.

B. THESIS STRUCTURE AND EXPERIMENT OUTLINE

The five chapters of this thesis outline the process undertaken to study and create new MEMS-based radiation detectors. It begins with this introduction and concludes with the results and analysis demonstrating the successful detection of neutron radiation. Following the Introduction, Chapter II discusses the physics and background of basic radiation principles and its interaction with matter. The chapter concludes with specific physical properties of dielectric materials and nanotubes. The discussion then moves to Chapter III, which provides a detailed outline of the fabrication process of each of the sensors used in the experiments. Because this thesis encapsulates three iterations of chip fabrication, data gathering and analysis, Chapter IV is a combination of both experimental methods and results. Each successive iteration was driven by the results of the last, so the choice to discuss them together is an effort to present the actual workflow as it transpired. Comments on the process as a whole and ideas for future work and applications of the technology are discussed in Chapter V.

The iterative approach described in Chapter IV was aided by ad hoc collaborations with NASA Ames Research Center and Lawrence Livermore National Laboratory (LLNL). The team at NASA provided expertise in sensor nanomaterials and sensor fabrication that allowed for a division of labor between sensor fabrication and testing/data analysis. The physical testing of the prototype sensors was conducted at LLNL. The access to a variety of neutron and gamma sources, and the expertise in their use, was instrumental in gathering the required data to refine iteratively until the objective was achieved.

II. BACKGROUND

In order to understand the working nature of the radiation detectors discussed in this thesis, it is important to understand both the basic interactions of radiation with matter and the various materials that alter those interactions. This chapter will address both subjects. First, on a broad scale, it will discuss two types of radiation and the ways they interact with matter. The second portion of the chapter will focus on certain materials and their specific responses to electromagnetic or neutron irradiation. It will also describe some of the important concepts required for the creation of the detectors themselves. The information in this chapter ultimately drives the decisions and design choices during the fabrication and testing of the sensors.

A. RADIATION BASICS

Radiation, at its most basic level, is traveling energy in the form of electromagnetic waves or energetic particles. Radiation originating from nuclear sources is further divided into one of two categories: charged particulate radiation or uncharged radiation. Charged particulate radiation typically refers to products of beta-type decay or alpha-type decay, either electrons or heavy charged particles. Uncharged radiation can be energetic neutrons or electromagnetic radiation. The following discussion will specifically address uncharged radiation, first as electromagnetic radiation in the form of gamma rays followed by energetic neutrons.

1. Gamma Radiation Properties and Interaction with Matter

Gamma radiation is an electromagnetic ray typically resulting from a nucleus relaxing from an excited state to its ground state or from an annihilation reaction. Gamma rays are the highest energy form of electromagnetic radiation, with energies beginning in the keV range but typically exist on the order of MeV for nuclear transitions [17]. That energy is carried by photons of wavelengths less than 1pm and frequencies greater than 10^{20}Hz, with lower wavelengths and higher frequencies leading to higher energy photons. For example, beta decay occurs when the nucleus of a radioactive atom emits an electron,

which leads to an atomic number (Z) increase of one, but leaves the nucleus in an excited state. Cobalt-60 undergoes beta decay according to the following process in Equation 1:

$$^{60}Co \rightarrow ^{60}Ni^{*} + e^{-} + \bar{\nu}_{e} \quad (1)$$

Following the reaction, cobalt's daughter nucleus, nickel-60, is left in an excited state, 2.505 MeV above its ground state energy. The newly formed nickel atom then emits two gamma rays, first at 1.173 MeV, then at 1.332 MeV, and finally settles in its ground state. This process is shown in Figure 3.

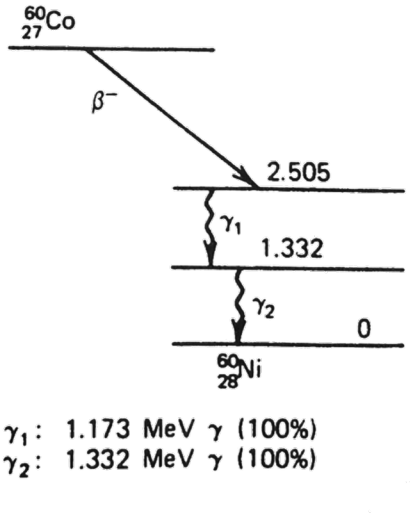

Figure 3. Cobalt-60 Radioactively Decaying to Stable Nickel-60.
Source: [14].

When photons in the gamma energy range interact with matter, they are either instantaneously absorbed or scattered off of an electron or a nucleus. For the purposes of radiation detection, the mechanisms of gamma photon absorption and scattering are photoelectric absorption, Compton scattering, and pair production [14]. In order to predict and analyze the response of different detector media to incident radiation of various energies, the methods of interaction and their probabilities must be understood.

(1) Photoelectric Absorption

Photoelectric absorption is the process by which a gamma ray is absorbed by an atom from which an electron is then ejected. The incoming photon interacts with an atom and transfers the totality of its energy to the atom. That energy is then applied toward the release of an electron from that atom and its resulting kinetic energy. The energy exchange of this process is governed by the equation:

$$E_{e^-} = h\nu - \phi \tag{2}$$

where E_{e^-} is the energy of the resultant free electron, h is Planck's constant, ν is the frequency of the photon, and ϕ is the minimum energy required to free the electron from the atom. Depending on the resulting energy of the free electron, it could interact with nearby atoms in the material or in the detector itself. Photoelectric absorption also creates an ionized atom, which, no longer in its preferred state, could also interact with nearby atoms. The probability of photoelectric absorption generally decreases as the incoming photon energy increases, with the exception of incoming energies that closely match the binding energies of the atom's electron shell and result in an energetically favorable state of the atom [14]. A probability graph of gamma-ray interactions is shown in Figure 4.

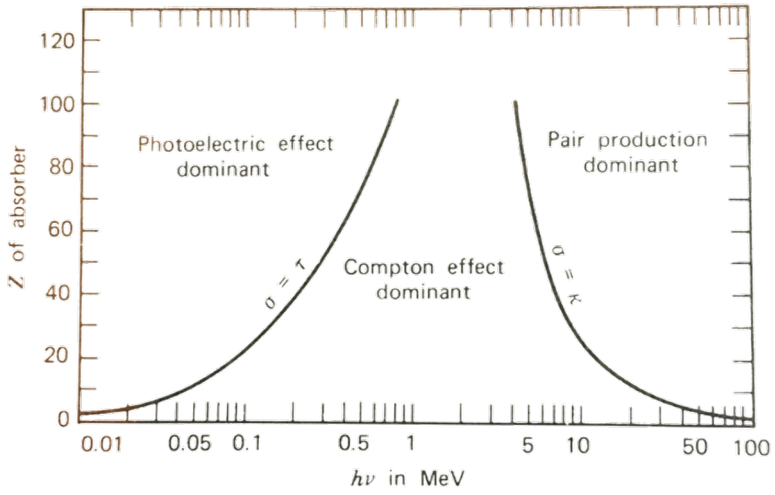

Figure 4. Relative Probability of Gamma Ray Interaction Mechanism. Source: [14].

(2) Compton Scattering

Compton scattering occurs when an incoming photon strikes a bound electron in the detection material. Unlike photoelectric absorption, the incident photon is not absorbed by the atom, but rather it is deflected off of the electron and continues its path through the detection material. Figure 5 shows the process of the incident photon striking an electron and scattering at angle θ, with the free electron scattering at angle ϕ.

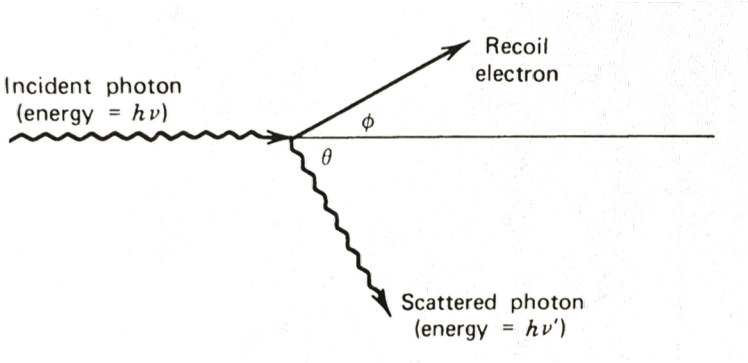

Figure 5. Depiction of Compton Scattering. Source: [14].

The photon maintains some of its initial energy because it is not completely absorbed by the atom. The new energy, *hv'*, is determined by Equation 3:

$$hv' = \frac{hv}{1 + \frac{hv}{m_0 c^2}(1 - \cos\theta)} \tag{3}$$

where m_0c^2 is the rest mass energy of the electron (0.511MeV). As the interaction material increases in atomic number (Z), the probability that a Compton scattering event will take place increases as well. Conversely, as the incoming photon increases in energy, the probability of Compton scattering decreases, shown in Figure 4 [14].

(3) Pair Production

Pair production occurs only when high-energy photons interact with materials. When a photon enters the electric field of a nucleus, the possibility exists (and becomes

more likely with higher energies) that the incoming photon can split into a positron and an electron. At a minimum, the incoming photon energy must exceed 1.02MeV, as the resulting positron and electron each have at least 0.511MeV rest energies, with all of the incoming photon's excess energy adding to the kinetic energy of the resultant particles. Following its creation, the positron will quickly annihilate with a nearby electron and produce two new photons in the secondary reaction, outlined in Figure 6.

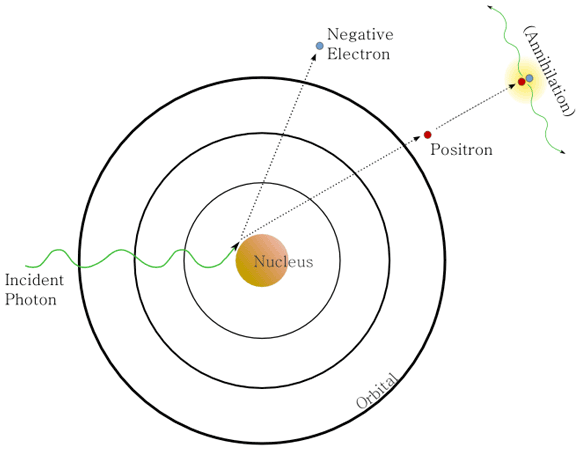

Figure 6. Pair Production Diagram. Source: [18].

2. Neutron Radiation Properties and Interaction with Matter

The neutron is an electrically neutral particle, so it possesses the ability to move unimpeded through areas of densely packed charged particles, including the atomic nucleus. This makes the neutron a prime candidate for the introduction of energy into an unstable nucleus. Fissionable sources are those that accept an energetic neutron into their nucleus in order to undergo fission, the high-energy splitting of the atom. These sources are necessary in the production of nuclear power and the creation of nuclear weapons. Fissionable sources execute a stochastic process of nuclear decay in which energetically unstable nuclei transition toward greater stability by emitting neutrons and other radiation products [19]. There are four fundamental types of interactions between these emitted neutrons and surrounding nuclei: elastic scattering, inelastic scattering, neutron absorption, and radiative capture [14].

(1) Nuclear Cross Section

The unique probability of an element interacting with an incident neutron, based on its energy level and its geometrical configuration, is referred to as the nuclear cross section. Nuclear cross section is specifically the quantification of the interaction probability of a particular nuclear reaction under particular conditions. A prominent theoretical physicist, Rudolph Peierls, who conducted his work during the early stages of nuclear theory, presented a clarifying analogy: "If I throw a ball at a glass window one square foot in area, there may be one chance in ten that the window will break, and nine chances in ten that the ball will just bounce" [20]. In this analogy, the window would have a $0.1ft^2$ "shattering" cross section, and a $0.9ft^2$ "rebound" cross section. Nuclear cross sections are most commonly reported in units of $10^{-24}cm^2$, known as "barns," and instead of shattering or rebounding, the cross sections refer specifically to the probabilities of the four fundamental neutron interactions discussed earlier.

Another crucial element of nuclear cross section, one not addressed by the analogy, relates to the energy of the incoming particle. The radiative capture reaction in particular is very sensitive to the energy of the incoming particle. Nuclei undergo this reaction more frequently for particular energies of incumbent radiation and so are "tuned" to these particular energy levels [20]. This property of a nucleus is referred to as "nuclear resonance."

The boron (n,α) reaction is of particular importance. Boron-10 (an isotope of natural boron) is an important element for neutron detection due to its ready availability and high neutron absorption (or radiative capture) cross section. Natural boron exists normally at roughly 80% boron-11, and 20% boron-10 by mass, but for neutrons in the thermal energy regime (approximately 0.025eV), the radiative capture reaction of boron-10 is roughly 3840 barns, which is nearly five times greater than that of natural boron, which is 790 barns [21]. Plots of these cross sections are provided in Figure 7 and Figure 8.

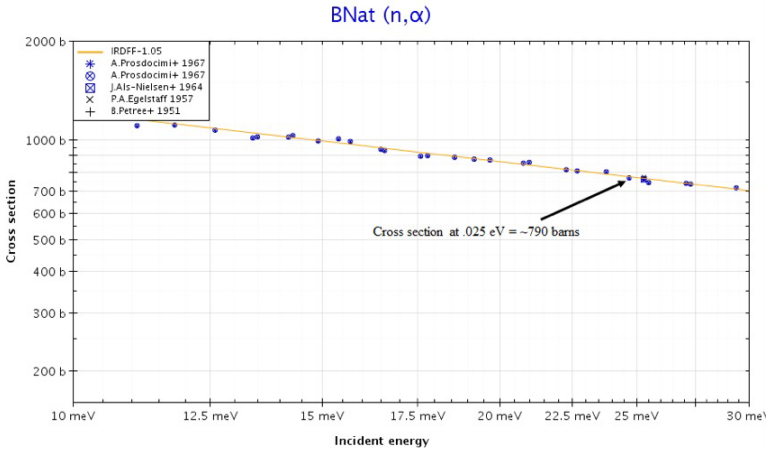

Figure 7. Nuclear Cross Section of Natural Boron. Source: [21].

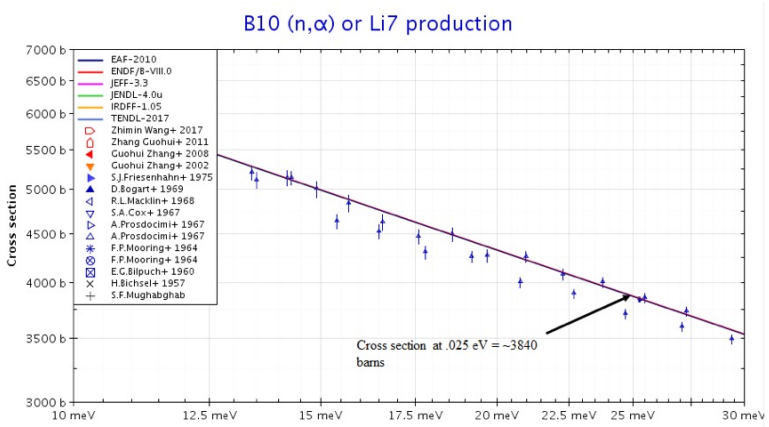

Figure 8. Nuclear Cross Section of Boron-10. Source: [21].

(2) Neutron Capture

Neutrons can be absorbed in several different reactions including (n,γ), (n,α), (n,2n), (n,p), etc. While the term "radiative capture" most commonly refers to the (n,γ) reaction, the present work focuses on boron as a neutron absorber so the (n,α) reaction requires further discussion. In this process, a nucleus absorbs an incident neutron and temporarily forms a "compound" nucleus. The newly formed compound nucleus then decays to its ground state via the emission of gamma radiation, similar to the reaction described in Equation 1. The capture boron-10 (n,α) reaction is represented for boron-10 in Equations 4 and 5 for an incoming thermal neutron, *n*:

$$ {}^{10}_{5}B + {}^{1}_{0}n \rightarrow {}^{7}_{3}Li + {}^{4}_{2}\alpha(6\%) \tag{4} $$

$$ {}^{10}_{5}B + {}^{1}_{0}n \rightarrow {}^{7}_{3}Li' + {}^{4}_{2}\alpha(94\%) \tag{5} $$

where *Li'* represents a lithium atom in its excited state. The high-energy products of the (n,α) reaction, and their specific contribution to neutron detection will be discussed further in Section B.2.c: "Nanotubes as Resistors".

The capture of the neutron and subsequent emission of an α particle, among other products, is the reason for the "(n,α)" nomenclature. This reaction is prompt, and yields a total product energy on the order of 2MeV. In the 94% probability case, the resultant lithium atom begins in its excited state. It then promptly decays to its ground state on a time scale of roughly 10^{-13} seconds by emitting a 0.48MeV gamma ray. Using the conservation of momentum principle, the resulting energies of the lithium atom and α particle can be determined. Since the incoming neutron energy is only 0.025eV, its initial momentum contribution is negligible. For the same reason, it is assumed that the α particle and lithium atom are emitted from the boron nucleus in opposite directions. To find the kinetic energies of the products, the following two equations are solved simultaneously (for the 94% case):

$$ E_{Li} + E_{\alpha} = 2.31 MeV \tag{6} $$

$$ \sqrt{2m_{Li}E_{Li}} = \sqrt{2m_{\alpha}E_{\alpha}} \tag{7} $$

The simultaneous solution of the equations yields energies of 0.84MeV and 1.47MeV of the lithium atom and α particle, respectively.

B. MATERIALS AND DETECTOR PHYSICS

To build a successful electronic nose, the correct materials must be selected as the "receptors" that will produce a clear and measured response to radiation exposure. Individual materials do not typically excel in specifically categorizing all types of radiation simultaneously. By selecting a group of appropriate materials, the radiation nose can be built with limited receptors, each with measurable and distinct responses to different types

of radiation. Since radiation sources have unique signatures in each form of radiation, selecting the correct materials to collect data separately yet simultaneously on each radiation type could yield a clear picture of the source by categorizing the full radiation spectrum produced.

Semiconductor and scintillator detectors are two prevalent types of solid-state detectors in use today. There are many materials being used and developed for both gamma ray and neutron detection, each of which comes with a unique set of applications and challenges [22]. Ideally, the electronic nose will take advantage of the unique applications of multiple materials while mitigating their disadvantages through the collaborative effort of the materials working in unison.

1. Capacitors and Dielectric Materials for Gamma Sensing

In order to test changing properties of detector materials, the first device used was a capacitor. Specifically, the capacitor dealt with the detection of gamma radiation interacting with a polymer dielectric material. The following sections describe the physics of a capacitor and the integration of sensing materials as dielectrics.

a. Fundamentals of Capacitor Physics

A capacitor consists of two charged conductors spatially separated from one another and held at equal and opposite charges. The measurement of capacitance, C, is a ratio of the electric potential between the conductors, V, and the charge stored on the conductors, q:

$$C = \frac{q}{V} \tag{8}$$

The measurement unit is the farad, F. A parallel-plate capacitor is the simplest form of a capacitor. It consists of two thin conducting sheets of area A, separated by a distance d. Using Gauss's law and the relation

$$V = -\int \mathbf{E} \cdot d\mathbf{l} \tag{1}$$

it can be shown that

$$C = \varepsilon \frac{\varepsilon_0 A}{d} \tag{10}$$

where ε_0 is the permittivity of free space ($8.85\times10^{-12}\ ^{F}/_{m}$) and ε is the relative permittivity or dielectric constant of an insulator used between the plates [23]. Because the capacitor sensor will be built without any moving parts, both A and d will remain constant, leaving ε as the only variable in Equation 10 that could lead to a measurable change in capacitance. The capacitors used in the MEMS sensor will be built on chips under $1cm^2$; even with maximizing the open space on each chip, the capacitance of each sensor is likely to be in the pF range, based on its geometry. Therefore, it will be important to find a dielectric material with a high ε in order to register a capacitance reading while taking measurements.

Dielectric materials increase capacitance by increasing the amount of charge, q, that can be stored on the capacitor's plates under the same electric potential, V. As shown in Figure 9, as an electric potential is established and increased across the plates of the capacitor, an electric field forms, orienting on the positively charged plate and terminating on the negative plate. Prior to the establishment of the electric field, the dipoles of the dielectric material are oriented randomly. When the electric field appears, each dipole of the dielectric material aligns in the opposite direction of the induced field, creating an opposing field that permits more charge to accumulate on the plates. Using Equation 8, if q is increased while holding V constant, C will also increase. ε then, is the ratio of the capacitance for a capacitor with dielectric material to the capacitance of one with none.

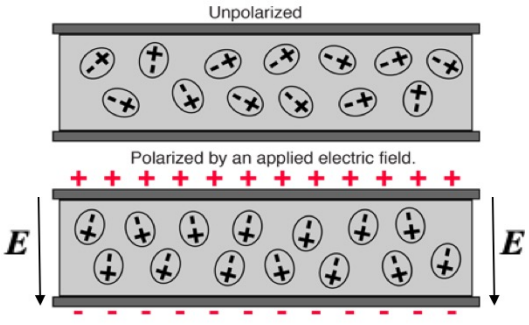

Figure 9. Dipole Orientation in a Dielectric Material with and without the Presence of an Electric Field. Source: [24].

b. Dielectric Materials for the MEMS Capacitor

In [8], Han et al. state that proper dielectric materials for a robust and versatile radiation detector should have "insulating properties, proper dielectric constant, dielectric strength, thermal stability, high purity, low moisture absorption, low viscosity, and responsivity to radiation." The PDMS used in their paper fit these criteria, but was responsive only to very high levels of radiation dose, as shown in Figure 10. PDMS provided a positive response for Han's group, but significant measurable change did not occur until about 10krad of absorbed radiation dose. To put that in perspective, an acute dose of around 500rad will likely kill a human without medical treatment [25]. In order to make the capacitor sensor sensitive to lower levels of radiation, different materials with similar detection qualities were explored.

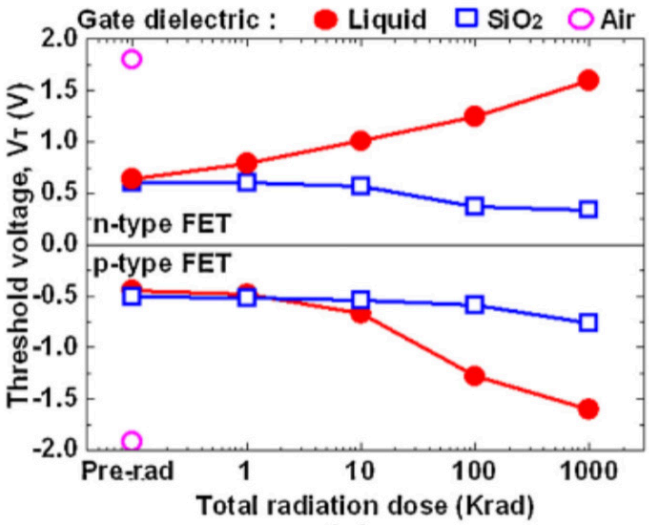

Figure 10. Response of PDMS (Red Line) to Total Radiation Dose.
Source: [8].

Due to the wide-ranging applications of radiation detection, as discussed in Chapter I, there is a plethora of materials with well-understood reactions to gamma irradiation. In order to meet the criteria outlined in [8], and to ensure ease of use and safety, the search was narrowed to gamma-sensitive polymers. Polymer gels have been used in the research and medical communities since 1992 as gel dosimeters, especially in the study of radiation

impacts on the human body [13]. These gels are usually studied as 3D dosimeters, therefore many of the well-established dose quantification techniques require magnetic resonance imaging or computer tomography [26]. Despite the range of polymer gels on the market or used in research today, there is a relatively small amount of research on the dielectric response of these gels.

Polyvinyl alcohol (PVA) is a water-soluble polymer used in medicine, papermaking, packaging, and as a bonding agent with little-to-no known negative toxicological effects [27], [28]. Due to its many uses and high production, it is readily available, inexpensive, and has a well-studied and defined response to gamma radiation [28]–[32]. The dielectric constant of PVA varies with temperature, solution properties, and frequency of the incumbent circuit. Work done by Van Etten et al. in [33] with different samples of PVA showed that at room temperature and low frequencies, the dielectric constant of PVA will typically be between ten and 15. That would lead to a desirable ε in Equation 10, and as discussed previously, is advantageous for taking reliable measurements. It is also common practice to add metal particles to polymers and other dielectrics to increase their dielectric constant and enhance their material properties, as noted by Shehap et al. in [28].

The most important aspect of PVA is its changing dielectric constant when exposed to gamma radiation. Both doped and pure PVA respond to gamma irradiation by increasing their dielectric constant. Through the interaction reactions discussed in Section A.1, gamma irradiation of PVA leads to rupturing and scission of the polymer chains and the chemical bonds that form the structure of the polymer. Free radicals are then created, leading to trapped charge carriers [30], and as discussed in [31], bonds inside the polymer are reformed, allowing for motion and realignment of the chains inside the polymer. Similar to PDMS, polymers also display their strongest response to radiation at very high radiation levels. Figure 11 includes a plot from Swu et al. [34] (on the left) showing the changing dielectric constant of polyacetate polymer (a similar substance to PVA) in response to gamma irradiation. The right side of Figure 11 shows the predicted theoretical response, using COMSOL modeling, of the MEMS capacitor sensor. While the response of the polymer at low doses of radiation is dwarfed by the large response at high doses, the

MEMS sensor will attempt to take advantage of the subtler changes toward the left end of the graph, which are in the hundreds of picoFarads, well within the measurement capabilities of a handheld multimeter.

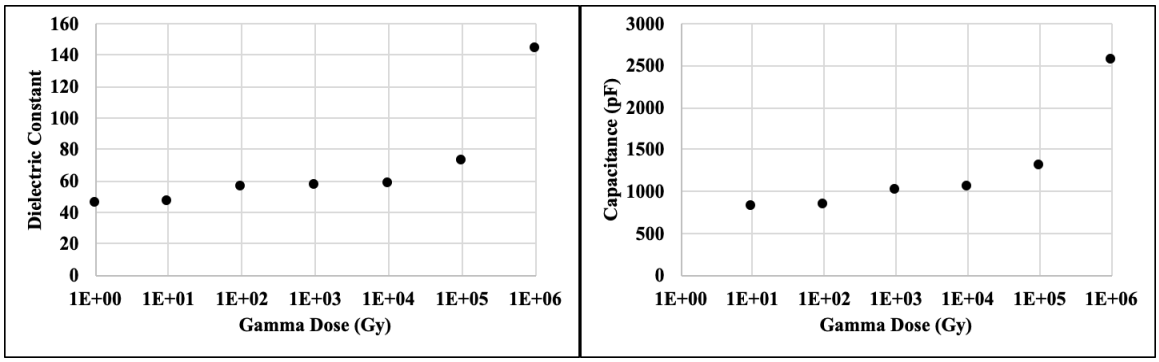

Figure 11. Plots of Theoretical Dielectric Constant and Capacitor Response. Source: [34].

2. Resistors and Nanotubes for Neutron Sensing

The second type of device used to test changing material properties were resistors. The resistive sensor took advantage of microfabrication techniques and nanotube properties of both carbon nanotubes (CNT) and BNNTs. By combining the materials onto a single sensor, they were used as resistive sensors, described in detail in the following sections.

a. Properties of Carbon Nanotubes

The advent of single walled carbon nanotubes (SWCNT) in the early 1990s began the exploration of a new arena of nanomaterial science. Sumio Iijima published [35] in 1991, a landmark paper outlining his successful creation of SWCNTs. Before his paper, as early as 1951, tube-like carbon nanostructures existed, but were largely dismissed as undesirable byproducts of other processes [36]. Iijima's reliable and repeatable formation of SWCNTs showed that they were not just waste products, but rather they served a purpose and could be applied to far reaching areas not thought of previously [36].

The structure of the CNT can be pictured by imagining a graphene structure of sp2 hybridized carbon atoms rolled onto itself and capped at the ends with hemi-fullerenes [36]. The lattice typically presents as a uniform hexagonal pattern along the nanotube, with a staggering array of possible variations in the morphology that can be introduced in order to amplify various aspects of the nanotube's performance, five of which are demonstrated in Figure 12. These variations involve, but are not limited to chirality, helicity, tube diameter, introduction of defects in the lattice, and many types of doping. Since the nose sensor will rely on the electrical properties of CNTs, the emphasis in the following paragraphs will be on variations that affect those electronic properties, namely the resistance.

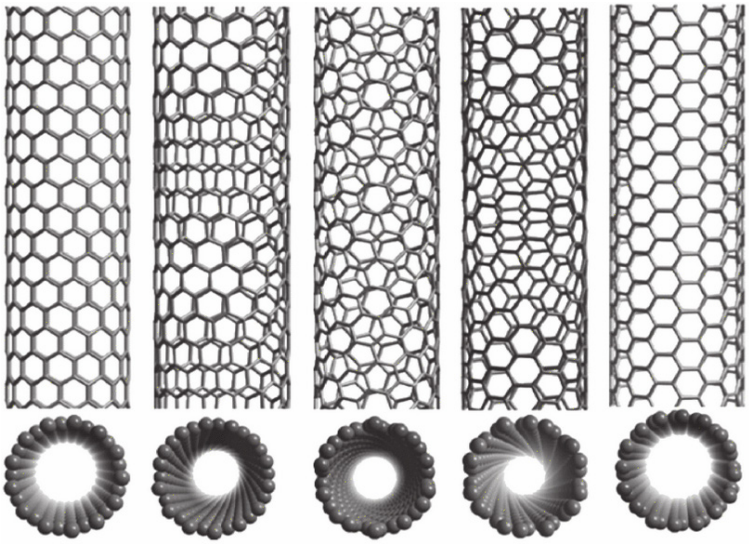

Figure 12. Carbon Nanotube Structures. Source: [6].

The layered SWCNTs to be used in the detector are a semiconducting graphene structure with a direct band gap on the order of 1eV. The small band gap is important because the low energy required to promote an electron to the conduction band will potentially enable faster and more accurate detection of radiation by allowing current to more readily travel through the CNTs. The 1eV band gap is not exact due to the non-trivial calculation of the inter-tube spacing of the bundle. The spacing is small enough that individual nanotubes are affected by the potential of neighboring tubes [36]. Despite

conducting quantum mechanical calculations using density functional theory, close correlation of predicted band gaps and observed band gaps of nanotube bundles remains an area for much improvement [37]. Figure 13 represents a general outline of density of states available versus Fermi energy differential for SWCNTs. Using the physical structure of the nanotubes planned for the detector (no chirality or helicity) and average tube diameter of ~1nm, the band gap can be approximated as ~1eV [38].

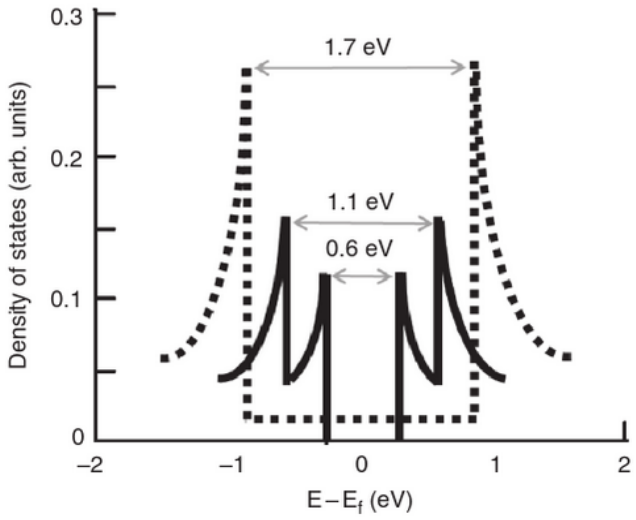

Figure 13. Density of States versus Fermi Energy Differential. Source: [36].

b. Properties of Boron-Nitride Nanotubes

BNNTs are structurally similar to CNTs in their hexagonal lattice and design. Boron and nitrogen atoms occupy lattice sites in an alternating pattern along the nanotube, as shown in Figure 14, where the dark sites represent boron atoms and the light sites represent nitrogen atoms. This alternation of the boron and nitrogen, as well as the more restrained morphology of the BNNTs (typically only hexagonal or rhomboidal) is due to energetic constraints on the configuration [36].

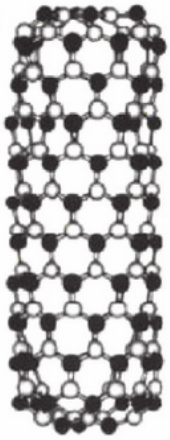

Figure 14. Hexagonal BNNT. Source: [6].

The use of isotopically pure boron-10 for the detector was of primary concern because of its high nuclear cross section relative to naturally occurring boron, as discussed in Section A.2(1). The nose detector will employ boron-10 BNNTs of the hexagonal morphology due to their ease of procurement and their decay products that result from neutron radiation, shown in Equations 4 and 5. Unlike SWCNTs, BNNTs have a large band gap that does not permit the flow of electrons so will not be used for their electrical properties. Instead, they will be used in nanotube form so that they can easily be mixed with the carbon nanotubes that provide the electrical pathways for the resistive sensor.

c. Nanotubes as Resistors

Nanotubes obey the basic properties of electrical resistance as macro materials in that resistance is characterized by ease of movement of charge through the medium. This movement of charge in semiconductor SWCNTs is accomplished through the promotion of electrons from the valence band to the conduction band of the material in the presence of an electric field. As discussed earlier, the SWCNTs' roughly 1eV band gap provides a relatively easy promotion of electrons from their valence band to their conductance band. BNNTs, with their larger band gaps, typically about 5eV [36], puts them in or near the regime of an insulator, severely restricting the movement of charge through their walls.

In order to capitalize on the nuclear cross section of the BNNTs and the conduction properties of the CNTs, the detection mechanism for the neutron sensor will be designed

as a type of solid-state scintillator. Neutron irradiation will likely cause the boron-10 in the BNNTs to undergo the neutron capture reactions in Equations 4 and 5, leading to the release of the high-energy lithium and α particles. The carbon-carbon (C-C) bonds that form the electric structure of the CNT resistor typically only have bond strengths on the order of 3.6-3.9eV [39]. Therefore, the high-energy products (0.84MeV lithium atom and 1.47MeV α particle) from the boron-10 (n,α) capture reaction should destroy many of C-C bonds they interact with. This should then create defect sites in the SWCNTs, inhibiting the flow of electrons and increasing the resistance of the SWCNTs.

THIS PAGE INTENTIONALLY LEFT BLANK

III. SENSOR FABRICATION METHODS

In order to detect the reactions described in Chapter II, two styles of sensor were built as the nose receptors. The first, a 16-pad sensor, allowed for the probing of 120 independent resistance paths during each measurement. The second, an interdigitated finger design, allowed for only one independent resistance measurement, but used all of the resistance paths available in that measurement. Two instruments were used as the brain for the sensor, an Arduino-style computer board and accompanying software, and two versions of a handheld multimeter. This chapter will describe the fabrication of the sensors and the application of sensor materials to them.

A. DESIGN AND FABRICATION OF THE 16-PAD SENSORS

The Elegoo MEGA 2560 board procured for this experiment, shown in Figure 15, was a low-power, low-cost computing board capable of executing simple commands continuously. Coupled with the 16-pad sensor and chip reader, shown in Figure 16, it could rapidly and continuously monitor all 16 pads and resulting paths of the sensor. The 16-pad detector operated as the brain for both the capacitive sensor and resistive sensor, each described in Chapter II. The resistive sensor used each unique path between the 16 pads by sequentially applying an electric potential difference across two different pads. It then measured the relative electric potential drop across the pads compared to a reference resistor in a voltage bridge. The total number of unique paths between pads was determined by

$$\sum_{i=1}^{n-1} n \tag{11}$$

where n was the total number of pads on the chip, so there were 120 independent paths for the 16-pad sensor. By including all possible paths between the pads, the chance of detecting a change on one of many different paths increased, but the chance of a large response declined based on attempting to detect the change individually instead of as a whole.

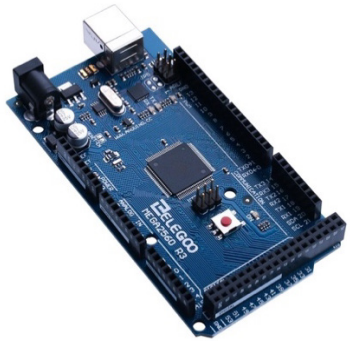

Figure 15. Elegoo MEGA 2560 Board

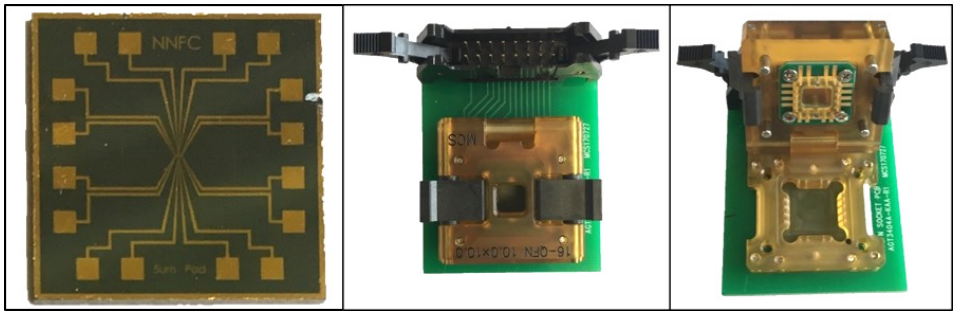

Figure 16. Example of a 16-Pad Resistive Sensor and the 16-Pad Chip Reader

1. NASA 16-Pad Resistive Sensor

The first version of the 16-pad resistive sensor was created using microfabrication techniques at NASA Ames. Shown in Figure 16, it measured 1cm x 1cm. Metal pads and contacts were layered onto an insulating substrate and connected to wires that led to the middle of the chip, where a nanotube solution was applied. The resistance across the 120 paths was measured at the center of the chip, where the fabricated wires came to an end, but were only connected by the nanotube solution. Figure 17 shows the termination of the on-chip wires and the nanotubes, where the dark areas on the chip are the applied nanotube solution. The nanotube solution in this iteration was also created at NASA and consisted of a mixture of semiconducting CNTs and natural BNNTs. It is important to note that the BNNT solution was not made with isotopically pure boron-10, but rather a mixture of roughly 80% boron-11 and 20% boron-10, therefore decreasing the overall nuclear cross section of the material discussed in Section II.A.2(1).

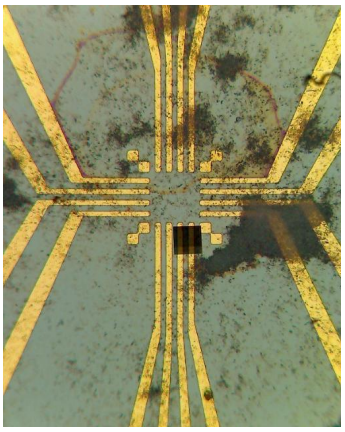

Figure 17. Middle of NASA Resistive Sensor with Nanotubes Applied

2. NPS 16-Pad Capacitive Sensor

The NPS 16-pad capacitive sensor was created in the NPS NanoMEMS Lab. It was created with the same dimensions as the NASA chip so it would also fit in the chip reader read by the Elegoo MEGA 2560. Like the NASA resistive chips, the capacitive chip also utilized wires to reach the sensor portion of the chip, but in this case, the sensor was a capacitor. SEM images of the completed capacitors are shown in Figure 18.

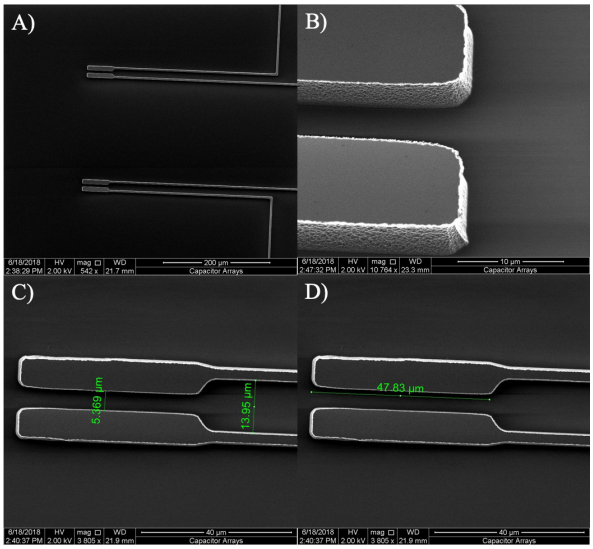

A) shows two capacitors with wires leading to their respective pads, B) shows a close-up view of an etched capacitor while C) and D) show the full capacitor view with dimensions.

Figure 18. SEM Images of the 16-Pad Capacitor Sensor

B. DESIGN AND FABRICATION OF THE INTERDIGITATED FINGER SENSORS

An interdigitated design takes advantage of a large electrode surface area while using only two electrodes on top of an insulating substrate. This design, shown schematically in its basic form in Figure 19, was used in both a resistive and capacitive sensor. For the capacitor, A in Equation 10 is maximized by using the total surface area of the overlapping fingers while d is generally a fixed distance between electrodes determined by the sensor design and microfabrication limitations. Once the walls of the capacitor are built, the dielectric material is then added in the electrode gaps to increase capacitance and serve as the detection medium. For the resistance chips, an electrical connection is established between the two electrodes by depositing nanotubes on top of the electrodes and bridging the gaps across many fingers.

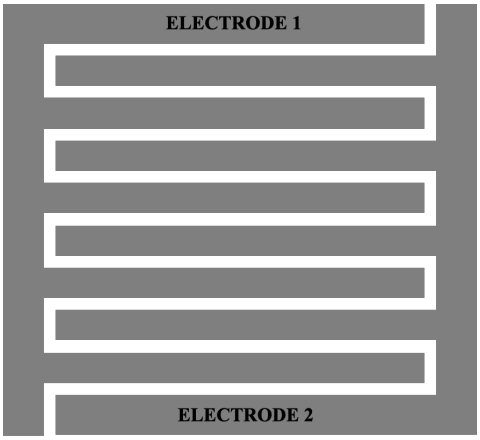

Figure 19. Design of an Interdigitated Finger Sensor

1. NPS Interdigitated Capacitor Sensor

The NPS interdigitated capacitor sensor was built on the NPS campus in the NanoMEMS lab. The chip itself was fabricated first, followed by the application of PVA for a dielectric material, and then was modeled and tested. Instead of building very small capacitors very close together, like on the 16-pad sensor, the interdigitated design was one big capacitor with a large surface area.

a. Wafer Fabrication Process

The interdigitated capacitor began with a 4in diameter silicon (Si) on insulator (SOI) wafer. The dimensions of the SOI wafer used for the capacitor were 100μm of Si on top of 5μm of insulating silicon dioxide (SiO_2). Starting with Figure 20, the wafer prior to any etching, the fabrication steps for the creation of a full wafer are listed below with accompanying MEMS Pro renderings (not to scale) where applicable:

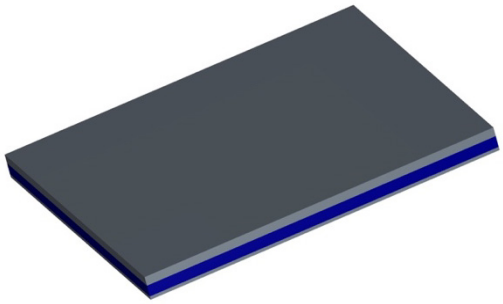

Figure 20. Si (Grey) on SiO_2 (Blue) Wafer

1. Deposit aluminum (Al) metal layer of thickness 100nm using Angstrom Engineering metal deposition machine.

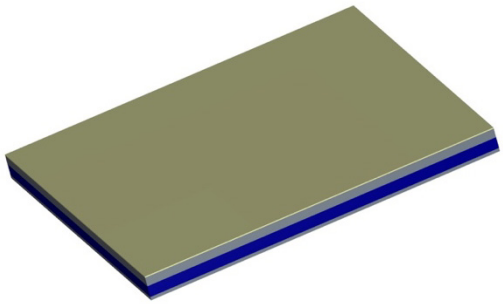

Figure 21. 100nm Al (Yellow) Deposited

2. Prime the wafer using the centrifugal application (spin-coating) of the organic solvent MCC 80/20 Primer at 3000 RPM with a ramp-up approach to final velocity.

3. Using the same centrifugal application technique, deposit a 10μm photo-resistive layer of SPR-220 at 1500 RPM for 40 seconds, then soft bake the wafer at 115°C for 90 seconds.

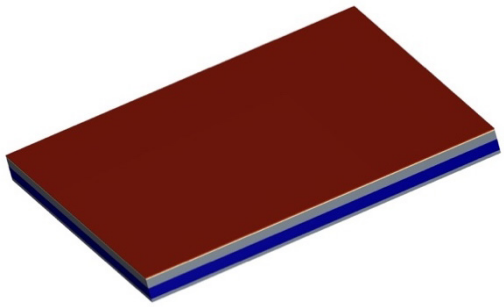

Figure 22. 10μm Photoresist (Red) Deposited

4. Using Canon Contact Mask Aligner, expose photo-resistive layer at 500 Integra for 44 seconds in order to etch photolithographic pattern onto wafer.

5. Allow wafer to rest for 30 minutes, then conduct post exposure bake at 115°C for 90 seconds.

6. Submerge wafer in CD-26 photo-developing solution for 240 seconds to remove exposed photo-resistive layer.

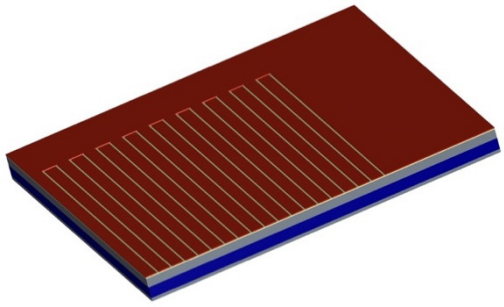

Figure 23. Exposed Photoresist Removed

7. Submerge wafer in Al etchant solution to wet-etch exposed Al. Leave submerged until all exposed Al has dissolved, typically 120 seconds.

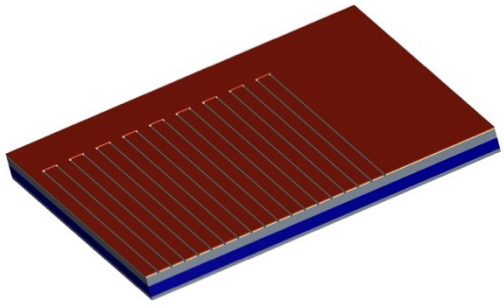

Figure 24. Exposed Al Etched

8. Conduct Bosch etching process for 210 cycles using Oxford Plasmalab machine to etch through exposed Si.

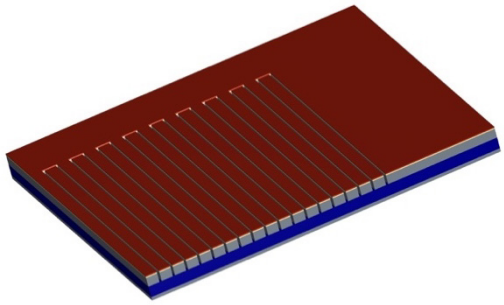

Figure 25. Si Layer Etched

9. Complete the process by removing the unexposed photo-resistive layer via centrifugal application of acetone and isopropanol at 3000 RPM for 30 seconds.

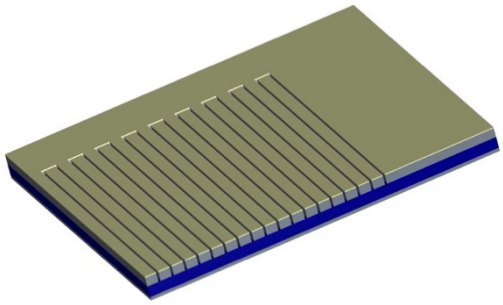

Figure 26. Remaining Photoresist Removed

A top-down image of the completed capacitor chip, taken from a scanning electron microscope (SEM) is shown in Figure 27. The figure is taken in the same corner as the model and shows the close spacing between electrodes created through the fabrication process. Figure 28 shows a cutaway side-view SEM image of the capacitor chip, with 100µm fingers on top of 5µm of SiO_2 (the rough textured area in the middle of the chip). Of note, at the base of the electrodes, a "notching" effect can be seen, described in [40], where the etching process chips away the base of the electrode.

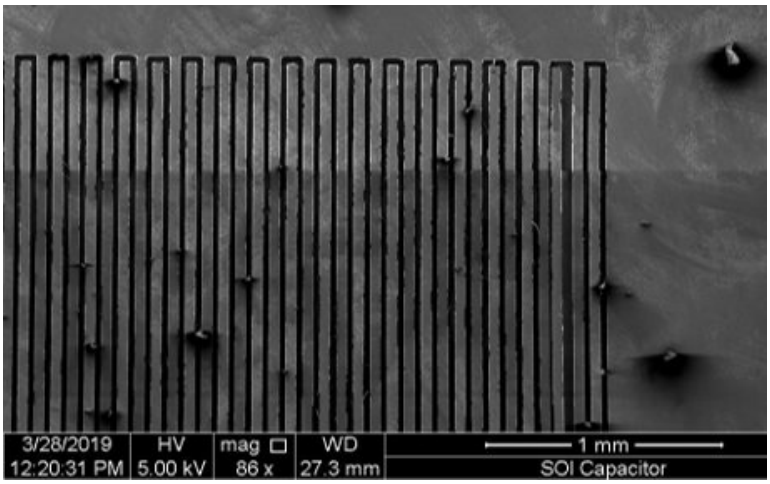

Figure 27. Top-Down SEM Image of Capacitor Chip

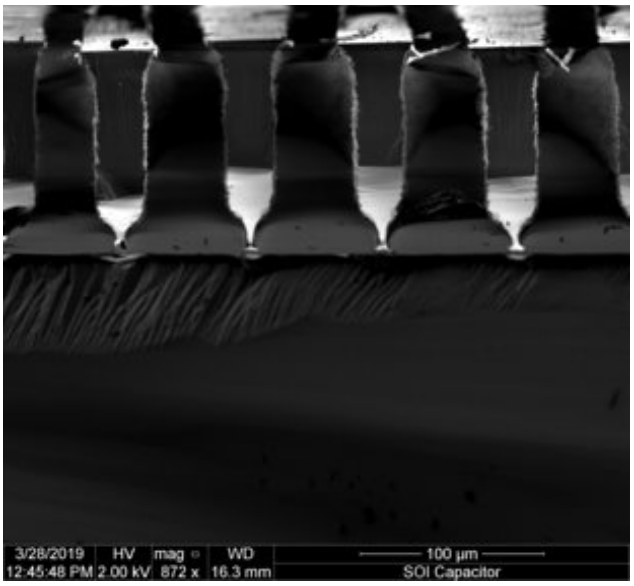

Figure 28. Side-View SEM Image of Capacitor Chip

b. Dielectric Application Process

Following the creation of the chips themselves, PVA solution was added as the dielectric material for the purposes discussed in Section II.B.1.b. The PVA solution, provided by NASA, was 5% by weight PVA powder dissolved in water. The team at NASA sealed the mixture in an airtight capsule for storage and transport to NPS to prevent its hardening prior to sensor application. In its original form, it was a clear liquid easily transferrable via pipette from capsule to chip.

In order to test the response of both pure and doped PVA, one-half of the solution was separated and doped with a 5mg/mL copper nanomesh in isopropanol solution provided from the NPS Materials Science Department. The final doped PVA solution contained 5% by volume nanomesh liquid. The rest of the PVA was left in its pure form. Both the doped and undoped PVA were applied to the chips via pipette transfer while the chips were heated for a fast and effective hardening of the solution. After heating a hotplate to 125°C, 75µL of undoped solution was applied to two sensors and 75µL of doped solution was applied to two sensors via pipette. All chips were placed on the preheated hotplate for eight minutes, until all PVA was solidified on the chips. Each was then removed and allowed to cool before post-bake measurements were made again, outlined in Chapter IV.

c. COMSOL Modeling of the Capacitor Chip

In order to test the feasibility of the capacitor sensor, a simple COMSOL model was created and run to find an expected capacitance measurement of the capacitor sensor. The model chip was built using an exported version of the final sensor design from MEMS Pro. The model is shown with a top-down view in Figure 29, following an evaluation holding the blue terminal at ground and the red terminal at +5V.

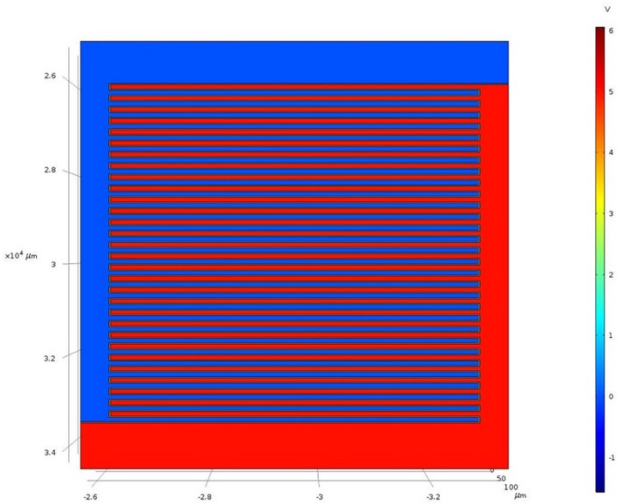

Figure 29. COMSOL Model to Test Interdigitated Capacitance

For the preliminary evaluation of capacitance measurements, the COMSOL Global Evaluation function was used with both Air ($\varepsilon = 1$) and PVA ($\varepsilon = 10$) as the dielectric material. With the sensor left in a vacuum for the measurement, air yielded a capacitance of 64.8pF and PVA yielded a capacitance of 226.1pF. Since both values were theoretically within the measurement potential of a handheld multimeter, the COMSOL model confirmed that the capacitor chip could be a feasible way to measure gamma irradiation.

2. NPS Interdigitated Resistive Sensor

The following two sections outline the creation of the NPS version of the interdigitated resistive sensor and the process required to create and apply the nanotubes as the sensing materials.

a. Wafer Fabrication Process

The NPS interdigitated resistive sensors were made on 4in diameter Si wafers with SiO_2 film deposited on top. The process, outlined below, was similar to the one described earlier in Section 1.a, but utilized Al as the electrodes and SiO_2 as the insulting layer, so did not require etching into the wafer. Beginning with the Si wafer:

1. Deposit SiO_2 either thermally or using plasma enhanced chemical vapor deposition.

2. Deposit Al metal layer of thickness 50nm using Angstrom Engineering metal deposition machine.

3. Prime the wafer using the centrifugal application (spin-coating) of the organic solvent MCC 80/20 Primer at 3000 RPM with a ramp-up approach to final velocity.

4. Using the same centrifugal application technique, deposit a 900nm photo-resistive layer of SPR-955 at 3000 RPM for 30 seconds, then soft bake the wafer at 90°C for 90 seconds.

5. Using Canon Contact Mask Aligner, expose photo-resistive layer at 9.63 mW/cm2 for nine seconds in order to etch the photolithographic pattern onto wafer.

6. Conduct post exposure bake at 120°C for 90 seconds.

7. Submerge wafer in CD-26 photo-developing solution for 40 seconds to remove exposed photo-resistive layer.

8. Submerge wafer in Al etchant solution to wet-etch exposed Al, leaving only Al pads and connections. Leave submerged until all exposed Al has dissolved, typically 120 seconds.

9. Complete the process by removing the unexposed photo-resistive layer via centrifugal application of acetone and isopropanol at 3000 RPM for 30 seconds.

b. Nanotube Application Process

Following the creation of the interdigitated resistor, nanotubes were deposited on the sensors. CNTs were dispersed into a solution of isopropanol and dropped onto the sensors using a 3mL transfer pipette. Isopropanol was chosen for its ability to evaporate quickly at room temperature, leaving only the CNTs on the sensor. Figure 30 shows SEM micrographs of the NPS resistive sensor. The larger figure exhibits the overlap of the CNTs on the interdigitated fingers while the pop-out image displays a further zoomed in photo of a group of CNTs, showing the strands of carbon used as the resistive structure.

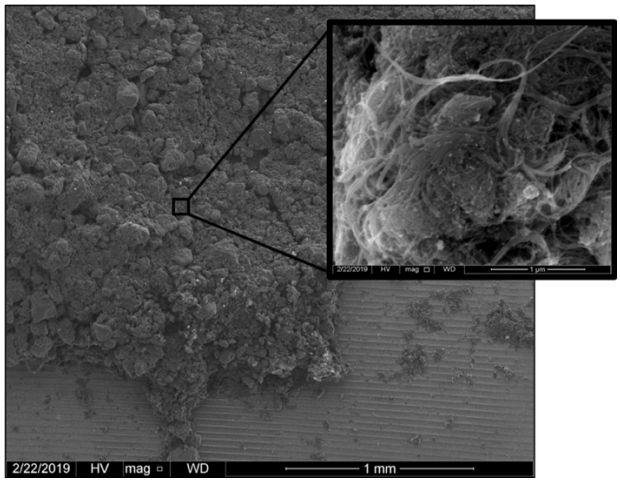

Figure 30. SEM Micrographs of the NPS Interdigitated Resistive Sensor

BNNT, LLC in Newport News, CA, provided 213mg of enriched (B-10) BNNTs, which required an additional process for their application onto the sensors. The production of the BNNTs by BNNT, LLC produced long strands of loosely bound together nanotubes that, together, resembled a group of cotton balls, shown in their original form and packaging in Figure 31. In order to convert the BNNTs in their original form to a usable solution, two approaches were used.

Figure 31. BNNTs as Received from BNNT, LLC

In the first approach, 4.4mg of BNNTs were placed in a 50mL glass vessel with 10mL of deionized water. An ultrasonic probe was inserted into the vessel and, utilizing a one second on/off pulse continuously for 20 minutes, dispersed the BNNTs into the solution by means of vibration. Figure 32 depicts the experimental set up for the first dispersion approach.

Figure 32. Ultrasonic Dispersion of BNNTs

In the second approach, 15mg of BNNTs were placed in a similar glass vessel, but this approach required the vessel be filled with 15mL of nitric acid. The mixture then underwent the same sonication technique described above for 60 minutes. A 150-minute reduction reaction at 130°C was then commenced using a recovery pipette, shown in Figure 33. The nitric acid was then separated from the BNNTs by spinning the vessel in a centrifuge at 4000 RPM for five minutes as shown in Figure 34. 5mL of demineralized water was added back into the vessel to make a new solution. The full details of this technique can be found in [41].

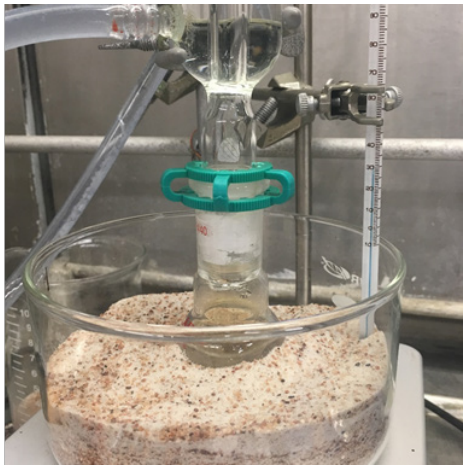

Figure 33. Nitric Acid Reduction to Disperse BNNTs

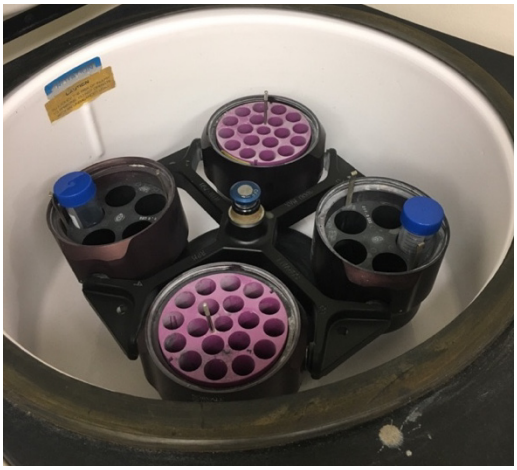

Figure 34. Centrifugal Separation of BNNTs

Once the BNNTs were in their aqueous solutions, they were applied to the resistive sensors on top of the CNTs already deposited. Similar to the CNT application, BNNTs were also applied via a microliter pipette. Since the BNNTs were dispersed in water, the wafer was heated on a hot plate to 100°C while the BNNTs were administered, shown in Figure 35. By keeping the hot plate at 100°C, the water dissolved quickly from the aqueous BNNT solution, leaving behind only deposited BNNTs.

Figure 35. Administration of Nanotubes

Shortly after testing the resistance of the newly created sensors, it became clear that heating the solution as it was applied caused a dramatic and permanent increase in resistance between the electrodes. Heating up the previously applied CNTs likely oxidized the nanotubes in the process, leading to an undesirable increase in their resistivity. The issue was remedied by evaporating the remaining water from the BNNT aqueous solution and replacing it with isopropanol. Much like the CNT application already described, the new BNNT solution was then deposited at room temperature. The isopropanol evaporated without the addition of any heat to the system, thus completing the nanotube application without unnecessarily spiking the resistance of the CNTs.

3. NASA Interdigitated Resistive Sensor

NASA fabricated three generations of resistive sensors that were used alongside the NPS sensors. The following paragraphs outline the design of the chips and the changes made in each generation.

(1) First-Generation Sensor

The NASA interdigitated resistive sensor was built on a flexible substrate with printed conductive ink electrodes, shown in Figure 36. After building the chip itself, a mixture of semiconducting CNTs and natural boron nanotubes were applied to the chips. In the first-generation NASA sensor, no additional boron-10 was applied to the sensor. This sensor used only natural boron nanotubes, thus drastically reducing the nuclear cross section of the sensing material, discussed in Section II.A.2(1).

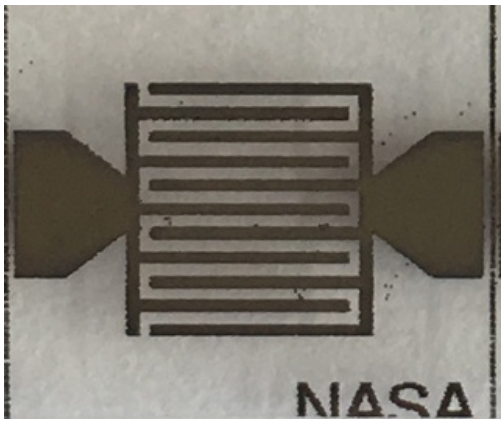

Figure 36. NASA Interdigitated Electrode Substrate

(2) Second-Generation Sensor

The second-generation NASA sensor added enriched boron-10 nanotubes to the first-generation sensor. Beginning with the sensor as received from NASA, then using the nanotube application process described in Section 2.b, the enriched boron-10 nanotubes were applied on top of the existing sensor and original nanotubes.

(3) Third-Generation Sensor

A third and final iteration of NASA sensors were created as a result of further experimentation, discussed in Chapter IV. These sensors began with completely new substrates created at NASA, and used a new set of CNTs and BNNTs. The substrates were identical to the prior generations, but the nanotube application process differed for the third-generation chip. NASA provided 40 sensors with three different solutions applied. The first 20 sensors used a combined CNT/BNNT solution created by mixing semiconducting CNTs and enriched BNNTs in water at a ratio of 1mg/mL (BNNT) and 0.1mg/mL (CNT). The next ten sensors were created by applying a BNNT-only solution to the chips. The final ten were created by applying a CNT-only solution to the chips. The final product of a third-generation NASA BNNT/CNT sensor is shown in Figure 37. The CNTs are conspicuous in the middle of the sensor and, although there are BNNTs also in the solution, their white color and relatively thin walls made them transparent when mixed with the CNTs.

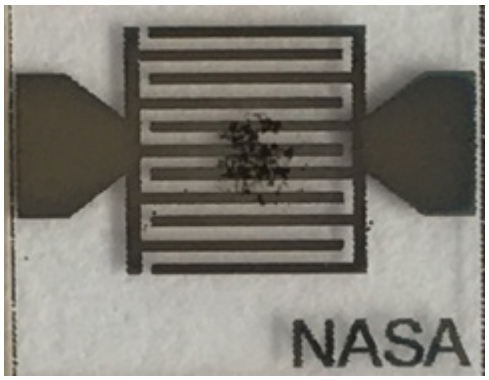

Figure 37. NASA Interdigitated Finger Sensor with Nanotubes Applied

THIS PAGE INTENTIONALLY LEFT BLANK

IV. EXPERIMENTAL METHODS AND RESULTS

Through three iterations of testing the created sensors, data analysis, and sensor modifications, this chapter will describe the path toward the creation of a successful radiation detector. Radiation testing for both gamma and neutron radiation was conducted at LLNL. Experimentation involved the exposure of the created sensors to various radiation sources in order to confirm the assumptions made in Chapter III. The total experimentation covered in this chapter occurred over three iterations, with each progressive iteration altered based on previous results. The success was borne from the iterative process of exposing sensors to radiation, reviewing the results, and improving those sensors for another round of testing. For this reason, the experimental methods and results are presented together in this chapter in an effort to reflect the actual process of the experiment.

A. ITERATION 1

The first iteration of testing did not produce successful results, but important discoveries were made during the creation of the original chips and their subsequent testing. This iteration began by using both the 16-pad and interdigitated chip designs but by the end of the iteration, the 16-pad design proved far less effective than desired. Iteration 1 began by measuring resistance changes with both the Elegoo MEGA 2560 board and a handheld multimeter, but the handheld multimeter was the only measurement method used going forward. The following sections outline the irradiation of the chips and the findings from the experiments.

1. Irradiation and Measurement Methods for Iteration 1

The NASA 16-pad resistive sensor and the NASA first-generation interdigitated resistive sensor were used exclusively in Iteration 1. As described in Sections III.A.1 and III.B.3(1), both sensor styles used CNTs as the electrical connection between electrodes and a layer of natural boron BNNTs on top of the CNTs as the detection medium. Three separate runs were conducted in this iteration. During each run, the sensors were exposed to a radiation source first in five increments of five minutes each, and then one long exposure of 30 minutes. After each exposure, either data was reviewed from the Elegoo

MEGA 2560 software program or resistance measurements were taken with a multimeter, depending on the chip style.

(1) Run 1: 16-pad Sensor with Unmoderated Californium-252 Source

The 16-pad sensor, inside the chip reader shown in Figure 16, was exposed to an unmoderated californium-252 source by placing it 7in away from the source. A schematic of the californium source is shown in Figure 38. The source itself, pictured in the foreground of Figure 39, irradiated the 16-pad sensor, shown in the background of the same figure. The sensor was housed in the chip reader and connected to the Elegoo MEGA 2560 with the voltage bridge circuit described in Section III.A.

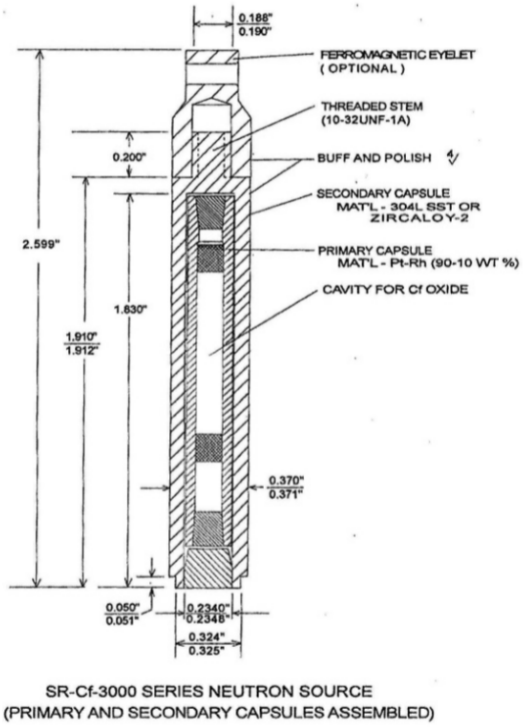

Figure 38. Cutaway of Californium-252. Source: [42].

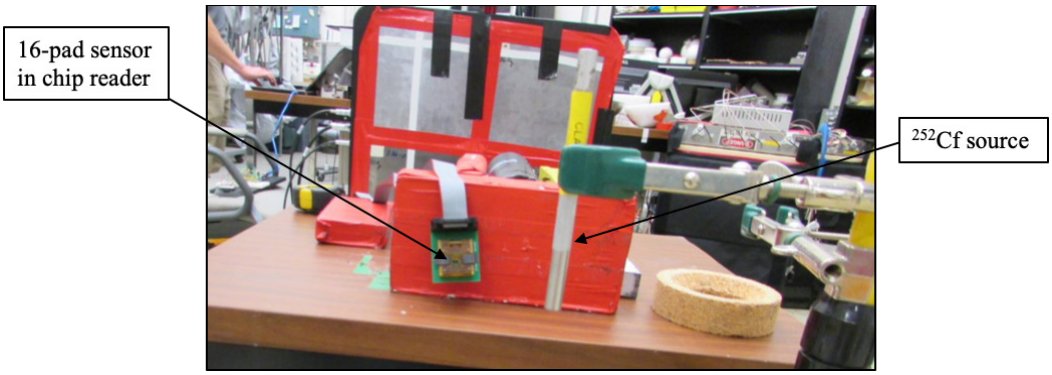

Figure 39. 16-pad Resistive Sensor Exposed to Unmoderated Californium-252 Source

The neutron emission rate of the californum-252 source was roughly 10^6 neutrons per second in a total 4π steradian solid angle. While the neutron fluence was high in Run 1, the average neutron energy was 2.13MeV, with a most probable single neutron energy of 0.7MeV [43]. The nuclear cross section, discussed in Section II.A.2(1), for natural boron and those high neutron energies, is only about one barn [21]. After completing the five- and 30-minute exposures, no change in resistance was recorded from the software program built to monitor the circuit and chip.

(2) Run 2: 16-pad Sensor with Moderated Californium-252 Source

In Run 2, the neutrons emitted from the californium-252 source were moderated by a 15cm diameter high-density polyethylene sphere. Figure 40 shows the modified experimental set up, with the chip reader secured to the surface of the sphere. This kept the chip nearly 7.5cm from the californium, as close as possible to the source while exposed to the maximum number of neutrons. The polyethylene shielding yielded a neutron fluence rate of approximately 2.6×10^3 neutrons per second in the desired thermal (0.025eV) energy regime [42], leading to a nuclear cross section of roughly 250 barns [21]. Despite the increase in detection probability, after completing five- and 30-minute exposures in the same manner as Run 1, no change in resistance was recorded from the software program built to monitor the circuit and chip.

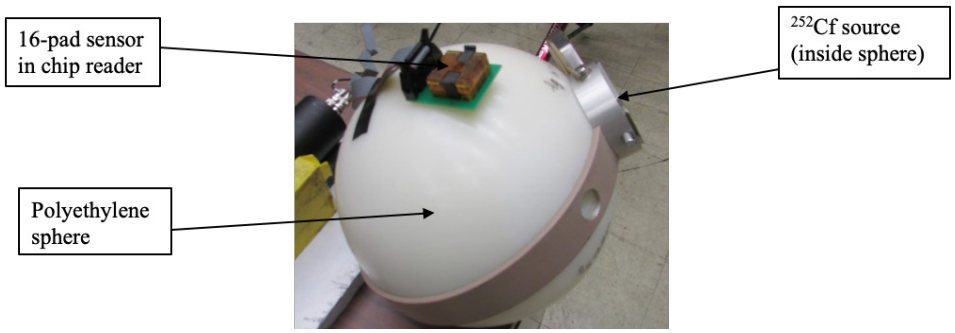

Figure 40. 16-pad Resistive Sensor Exposed to Moderated Californium-252

(3) Run 3: 16-pad and Interdigitated Sensors with Deuterium-Tritium (DT) Neutron Generator

For the final run, both the 16-pad and interdigitated sensors were exposed to neutrons from a DT neutron generator. The generator created an ionized beam of deuterium that was accelerated across an electric potential of about one MeV. The deuterium ions then collided with a tritium saturated titanium target where they underwent the deuterium-tritium fusion reaction:

$$^{2}H + ^{3}H \rightarrow ^{1}_{0}n + ^{4}He \tag{12}$$

and released a high fluence (~10^{8} neutrons per second) of nearly identical 14.1MeV neutrons. Due to the very high energy of the neutrons, the DT neutron generator was moderated using a hollow, high-density polyethylene cylinder of 2in wall thickness, 5.375in in length, shown in Figure 41.

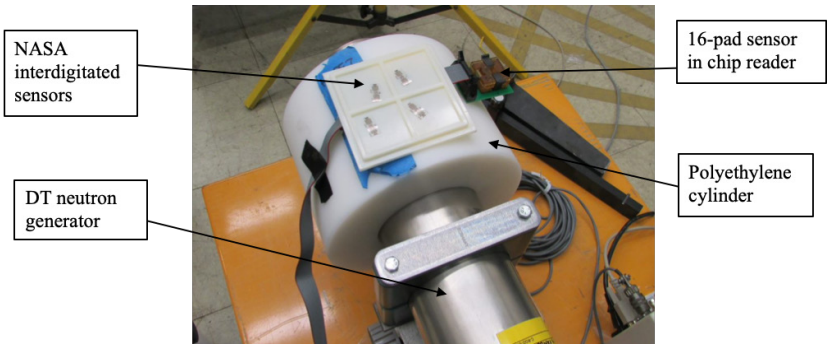

Figure 41. Sensors Exposed to DT Neutron Generator

Due to its high neutron rate and the power of the source, only one five-minute run was conducted which provided sufficient exposure for the chips. After the exposure, the interdigitated sensors were probed using a Fluke 179 multimeter, and the 16-pad sensor was tested with the same Elegoo MEGA 2560 board and software as used in Run 1 and Run 2. Similar to the previous runs, the neutron generator did not produce any measurable change in either the interdigitated sensors or the 16-pad sensor.

2. Discussion of Iteration 1 Findings

Iteration 1 did not produce measurable changes in resistance for any type of sensor tested or source used. Due to its small cross section and subsequent lack of response to irradiation, natural boron was deemed ineffective as the sole detection source for thermal neutrons. The probability of natural boron undergoing the necessary capture reactions on a large enough scale for detection with the devices used was too small for the early stages of sensor design. Due to unnecessary circuit complexity and lack of measurement fidelity, the 16-pad sensor design would also no longer be used after Iteration 1 as it was not a viable option for initial materials testing and categorization of sensor response.

B. ITERATION 2

Iteration 2 confirmed that, as theorized, enriched BNNTs were more effective than natural boron BNNTs for neutron radiation detection. The capacitor chips were tested in Iteration 2 for the first time but did not produce any significant results. After making the changes necessary to the resistive chips from the results of Iteration 1, the sensors and measurement techniques of Iteration 2 produced results that drove one more round of sensor refinement and testing. Analysis of the results also mandated extra testing to determine the chips' response to light. This further testing and analysis discovered that the sensors responded to light by decreasing the resistance measured across electrodes, an important result that drove the chip design in Iteration 3.

1. Irradiation and Measurement Methods for Iteration 2

Since the lack of neutron radiation detection in Iteration 1 was likely due in part to the low cross section of natural boron, boron-10 enriched BNNTs were added to all neutron

detector chips used in Iteration 2. The NPS interdigitated resistive sensor (Section III.B.2), the NASA second-generation interdigitated resistive sensor (Section III.B.3(2)), and the NPS interdigitated capacitor sensor (Section III.B.1) were all used in Iteration 2. Both resistive sensors used the boron-10 enriched BNNTs and the capacitor sensor was added in separate runs to test for gamma irradiation response. The first run was conducted using five-minute exposures of the sensors to neutron radiation. Following those exposures, an additional one-hour exposure was conducted. The gamma radiation measurements were conducted in two successive exposures of 30 minutes each.

The radiation sources used in this iteration were a plutonium-beryllium (PuBe) source for neutron radiation and a cobalt-60 source for gamma radiation. The switch to the PuBe source from the californium-252 source for neutron radiation was based on the neutron fluence rate of roughly 10^7 neutrons per second for PuBe compared to the lower rate of 10^6 for californium-252. Since the goal of the experiment at this stage was to elicit any response from the detector, the highest fluence of thermal neutrons was desired in order to show whether the materials used were viable options as detection media.

(1) Run 1: NASA and NPS Resistive Sensors with PuBe Source

In order to create thermalized neutrons, the PuBe source was moderated by 10cm of high-density polyethylene. The set up resembled that shown in Figure 40 and Figure 41. The PuBe source came in the form of a canister approximately 6cm wide and 12cm high, so the polyethylene sheet was set atop the canister and the interdigitated resistive sensors were placed atop the sheet. The NPS interdigitated resistive sensors and the NASA second-generation interdigitated resistive sensors were tested simultaneously. The chips were exposed to the radiation with the same five-minute exposure time scheme used in Iteration 1. Resistance measurements were recorded by hand after probing each chip with the Fluke 179 multimeter and are shown in Table 2 in Section (3).

The NASA chips demonstrated what seemed to be a consistent change in response to neutron irradiation. Table 1 shows the resistance measurements of all eight NASA chips following each exposure for the first 30 minutes. The pre-radiation measurements were taken over the course of one week at NPS prior to exposure at LLNL. Each NASA chip

decreased in resistance as the experiment continued, suggesting a decrease in conjunction with increasing neutron irradiation. Due to the difficulties in controlling the CNT/BNNT nanotube bundles' exact shape and configuration, the pre-radiation resistances of detectors fell in a range of values. For ease of result display, each chip's measurements were normalized to their pre-radiation averages and averaged together in Figure 42, which shows a resistance decrease of almost 50% over the 30 minutes of exposure.

Table 1 Resistance Measurements from NASA Interdigitated Sensors for Iteration 2, Run 1.

			Resistance Post-Exposure (Ohms)						
Chip Name	Average pre-radiation resistance (Ohms)	Standard deviation (Ohms)	0 minutes	5 minutes	10 minutes	15 minutes	20 minutes	25 minutes	30 minutes
Chip 1 Left	536.375	46.65	483	322	296	268	261	239.2	234.2
Chip 1 Right	23748.75	6164.53	28900	10780	9400	8450	7790	6930	6250
Chip 2 Left	372.20	115.12	356	259.7	237.3	219.9	205.4	192.2	181.9
Chip 2 Right	240.56	50.00	238	159.7	145	134.6	125.5	118	111.6
Chip 3 Left	39.21	2.24	38.7	26.97	25.18	24.06	23	22.18	21.42
Chip 3 Right	14.76	0.82	14.6	11.82	11.27	10.8	10.47	10.13	9.82
Chip 4 Left	9.61	0.97	9.33	7.47	7.04	6.73	6.52	6.29	6.16
Chip 4 Right	12.81	1.11	13.3	9.92	9.17	8.68	8.39	8.09	7.88

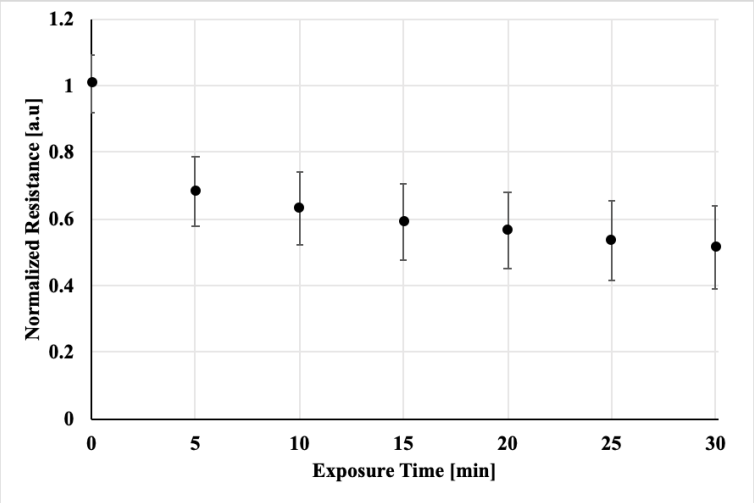

Figure 42. NASA Chips Decreasing Resistance During Iteration 2, Run 1

Following the initial 30 minutes of exposure time, the NASA chips were placed back in their original boxes and not probed again for over an hour. When the chips were

being prepared for another exposure, it was discovered that all of the resistances had increased. The resistance readings on every chip following the storage time increased from their post-exposure readings by at least 13%, and the longer they were left in their packaging, the more their resistance increased. Further testing conducted at LLNL discovered that when the chips were exposed to the environment by taking them out of their packaging, even with no radiation source present, their resistance consistently decreased. When the chips were then placed back in their packaging, the resistance increased back toward its original pre-radiation values. Figure 43 shows the averaged and normalized responses of the eight NASA chips after a period of being subsequently uncovered (blue points) and then covered (orange points). There was a clear and repeatable resistance change connected specifically to the exposure to, or protection from, the environment.

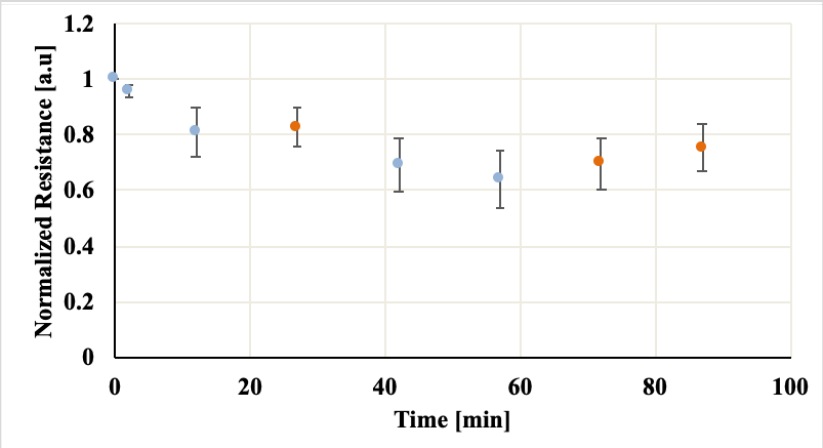

Figure 43. NASA Chip Response to Environment

(2) Run 2: NPS Interdigitated Capacitive Sensors with Cobalt-60 Source

The NPS interdigitated capacitors with both doped and undoped PVA were exposed to an unshielded cobalt-60 source for two prolonged 30-minute exposures. Each chip was tested before and after irradiation with a BK Precision 875A multimeter, but no change in capacitance was detected.

(3) Run 3: Long Exposure of NPS Interdigitated Resistive Sensors with PuBe Source

Following the short exposures in Run 1, the NPS resistive chips were exposed to two long, continuous exposures to the PuBe source. The first was a 60-minute moderated exposure and the second was a 30-minute moderated exposure. After the first 25 minutes of measurements in Run 1, there were no clear trends in the resistance changes. In order to test for any response, the attempt was made to saturate the chips with a high total number of neutrons to elicit a clearer response. Table 2 shows an example of the measurements taken on a portion of the chips. The specific chips used in Table 2 were from one of the three wafers created for Iteration 2, and are consistent with the results across the spectrum of all the chips tested. The pre-radiation measurements were taken over the course of one week at NPS prior to exposure at LLNL. The data collected did not show any universal correlation between exposure time and change in resistance.

Table 2 Resistance Measurements from NPS Interdigitated Sensors for Iteration 2

			Resistance Post-Exposure (Kohms)							
Chip Name	Average pre-radiation resistance (Kohms)	Standard deviation (Kohms)	0 minutes	5 minutes	10 minutes	15 minutes	20 minutes	25 minutes	85 minutes	115 minutes
C1	90.33	3.36	99	97.8	93.8	99.2	102.3	105.7	95.2	90.3
A3	84.58	5.91	80.3	87.7	86.6	86.7	88.9	91.1	87.4	87.4
C3	26.75	0.73	27.7	28.2	28.2	28.1	27.8	27.8	27.9	27.1
A4	41.00	2.28	38.5	38.1	38.6	38.6	140.3	137.5	153	153
C4	1.60	0.40	1.41	1.4	1.4	1.4	1.4	1.39	1.401	1.402
D4	524.00	41.16	472	457	456	454	474	500	477	477
C5	28.93	0.66	29.2	29.2	28.7	28.5	29.6	29.8	31.6	30.1
A6	18.08	0.89	17.5	17.2	17.4	17.3	16.5	16.5	17.4	16.9
C6	17.73	1.82	19.6	18.2	18.6	18.6	18.4	17.9	18.6	19.4
L1	40.80	0.44	40.4	40.8	40.8	40.6	36.5	36.41	39.5	39.9
L2	13.00	1.00	14.9	14.4	14.1	13.8	13.6	13.4	13.3	11.9
L3	35.85	9.92	39.6	39.3	39.2	38.6	40.2	40	38.5	38.7

Contrary to expectation, some chips increased in resistance while others decreased, while still others remained within the mean plus standard deviation from pre-exposure measurements. During the data analysis of all of the chips, ten in total stood out as having resistance values that either consistently increased or consistently decreased during the exposures. Figure 44 and Figure 45 are graphical representations of the two groups of chips. The wide range of results described were cause for further investigation because, as discussed in Section II.B.2.c, the resistance of the chips was expected to increase in

response to neutron irradiation through the decay products of the enriched BNNTs creating defect sites in the underlying CNTs.

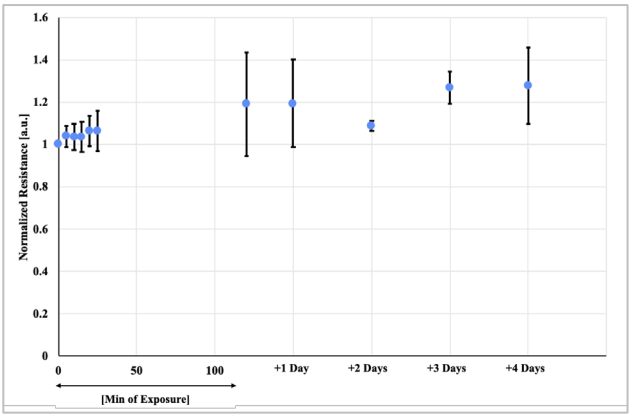

Figure 44. NPS Sensors with Increasing Resistance

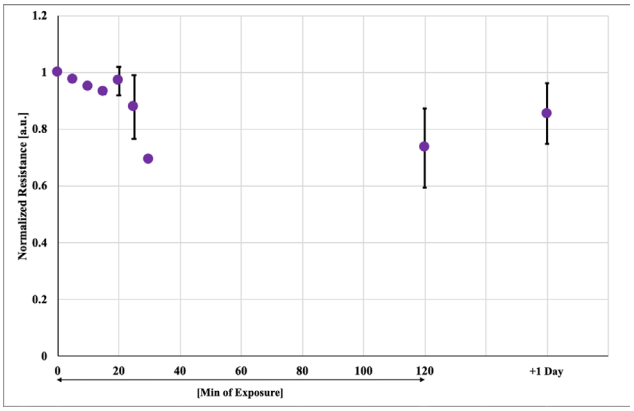

Figure 45. NPS Sensors with Decreasing Resistance

2. Categorization of Environmental Response

The data analysis of Iteration 2 showed that further investigation into non-radiative effects on the chips was needed in order to isolate those effects from future testing. Ultimately, it was shown that light exposure likely drove the unexpected results. The two groups of unexpected data, the NASA chips' resistance response to the environment and the different grouped responses of the irradiated NPS chips, were not predicted by the initial baseline measurements or the initial theories. Initial testing likely missed the light

response of the chips because only one set of measurements was taken per day, so continued changes as chips were left out of their packages were not captured. The initial measurements were taken in various temperatures and humidity levels, which were repeated post-exposure, but that was found not to have a major impact on resistance response.

The first post-exposure measurements focused especially on changes induced by fluctuations in temperature and humidity, but after comparing these measurements to those taken before the Iteration 2 experiments, temperature and humidity changes seemed to produce insignificant changes in resistance. Because of the chips' relatively quick response to their removal from packaging, the next measurements focused on the interaction of light with the sensors. Previous work has shown that CNTs can be used as infrared (IR) light detectors [44], and since CNTs were the conducting medium of the sensors, an experiment to verify the effect of light on the interdigitated sensors was prepared.

In order to conduct the experiment, a station with precise probing equipment was wired into a voltage divider circuit and connected to a LabView program that monitored resistance changes. A photodetecting diode was also simultaneously monitored to collect data on light intensity at the site of the chip. A NASA interdigitated sensor, already used in the testing at LLNL, was placed on the probe station under a light source, where its resistance change could be continually monitored by the probes. The apparatus and set up is shown in Figure 46.

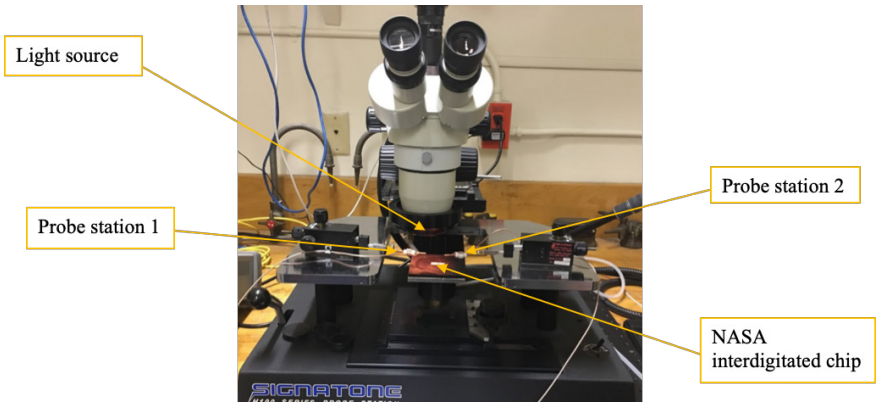

Figure 46. Probe Station Set Up for Light Interaction Experiment

Using the continuous and simultaneous recording capabilities of the LabView program, the light intensity was swept from zero light to maximum intensity while recording the resistance of the sensor and the light intensity. This was repeated for five different NASA chips and the results from a sweep of light on and off is shown in the plot in Figure 47. The plot confirms that the decrease in resistance witnessed at LLNL was very likely the result of interaction with light.

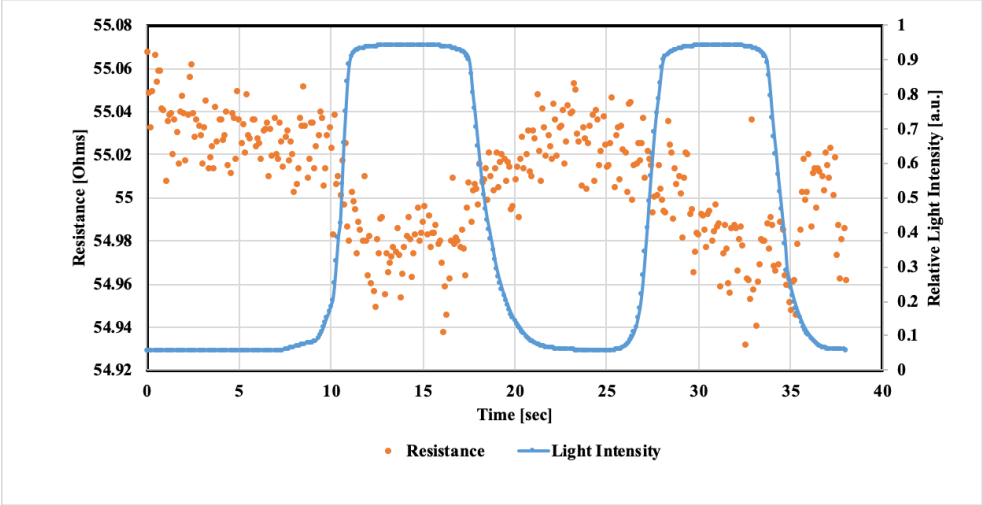

Figure 47. Resistance Response of NASA Chip to Light Exposure

3. Discussion of Iteration 2 Findings

The following paragraphs summarize the findings of the Iteration 2 experiments and outline some of the changes made before moving to Iteration 3.

(1) Gamma Detection

The NPS interdigitated capacitor detector did not produce a measurable change in capacitance. This could have been due to three things: no change in dielectric constant, not a large enough change to be detected by the BK Precision 875A multimeter, or issues with the chip design. After further modeling with COMSOL, shown below in Figure 48, a major contributor to the null result was likely the chip design. First, there was unwanted capacitance between the electrodes and the substrates, shown by the red arrows in the figure

representing electric field lines. There are field lines between the desired electrodes, but at the bottom of the figure there are also vertical lines displaying the parasitic capacitance between the interdigitated fingers and the substrate below. Second, the chip design and etching process led to possible unstable electrodes, noted in Figure 28, built very close together. If the fingers of the electrodes were perturbed and broken, a connection across electrodes was made, causing an unreliable measurement.

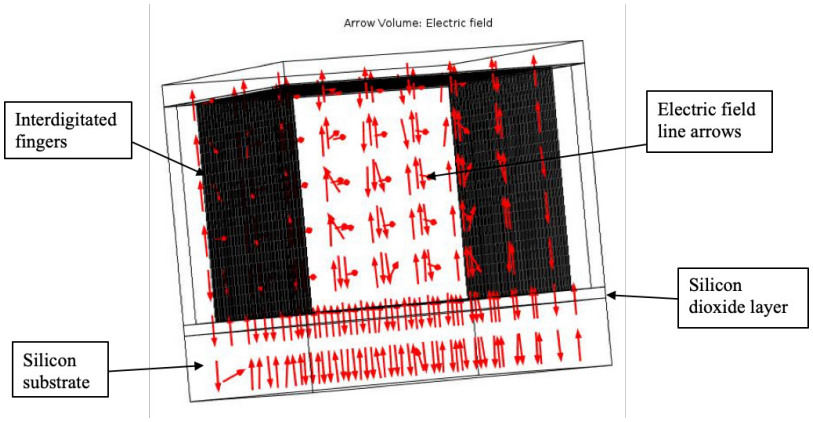

Figure 48. COMSOL Model of Electric Field Lines in Capacitor Chip

(2) Neutron Detection

The results from Iteration 2 did not imply a successful detector had been created, but it did provide valuable insights for chip design going forward. Most importantly, it demonstrated the feasibility of a neutron detector using boron-10 enriched BNNTs. The mixed and varied data shown in Table 1 and Table 2 led to a crucial discovery regarding the light response of the CNTs on the chips. By categorizing the light response, shown in Figure 47, the resistance decrease of the interdigitated sensors was confirmed as stemming from the light outside of its packaging. Despite being exposed to a wide light spectrum for its testing, it is likely that the chips' resistance decreased mostly due to IR light. Their packaging was clear enough to allow visible light to pass through, but was mostly opaque to IR light and prior work done in [44] supports this hypothesis.

The mixed results of the NPS resistive sensors outlined in Figure 44 and Figure 45 may have been a result of light and radiation interactions. The decrease in resistance seen

in some of the sensors was likely due to the effects of light interaction overcoming either small or non-existent neutron radiation effects, and the sensors that exhibited an increase in resistance likely experienced neutron radiation effects overcoming light interaction effects. An issue in Iteration 2, seen in Table 2, was the inherent measuring error when using NPS chips. The dimensions of the chips were identical to the interdigitated design used for the capacitor, seen in Figure 29. Therefore, the electrodes used to probe the resistance measurements had a relatively large area compared to the probes, so each measurement could not be made precisely each time. Because of this, NPS chips were not used in Iteration 3.

C. ITERATION 3

Changes made to the chips from the analysis of Iteration 2 results led to success in Iteration 3. After exposing the chips to radiation again at LLNL and verifying the results, Iteration 3 produced chips whose resistance consistently increased in response to neutron irradiation.

In the previous iterations, the most consistent measurements came from the NASA design of the interdigitated sensors. NASA's nanotube application technique allowed them to deposit smaller and more precise quantities of nanotubes compared to the NPS technique. The NPS technique, depositing with a pipette, outlined in Section III.B.2.b, left mounds of nanotubes roughly 0.3mm in height, where the NASA chip deposition technique resulted in mounds only 0.05mm high. The larger mounds of nanotubes on the NPS chips may have resulted in reactions that occurred only in the uppermost layers of the sensor, not allowing the reaction products to reach the CNTs lower on the sensor, which were responsible for the electrical path between the electrodes. Since the enriched boron-10 BNNT solution seemed to be an effective detector material, the enriched BNNT solution was provided to the NASA team who mixed it with semiconducting CNTs and applied it to their interdigitated substrate on the NASA third-generation sensor.

The housing for the Iteration 3 sensors is shown in Figure 49. There were four separate sensors in the clear housing, with three different nanotube mixtures across them. The top two sensors contained a mixture of CNTs and BNNTs, the third sensor contained

only BNNTs and the fourth sensor contained only CNTs. Instead of probing the chips directly with a multimeter like in the previous iterations, wires were secured to the chip pads with conductive tape and staples. Finally, the four-chip array was housed in a clear plastic container that was mostly opaque to IR radiation.

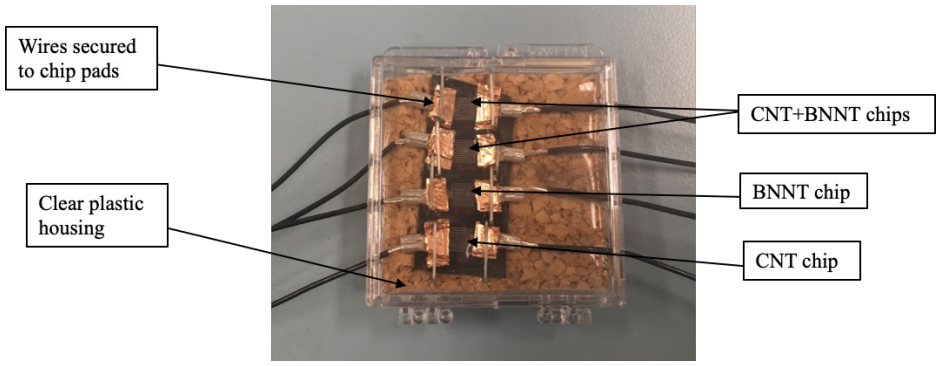

Figure 49. Iteration 3 Sensor Housing

In total, 36 chips were measured, separated into nine separate housings. Because a large number of chips would be irradiated simultaneously, a system for organizing the leads for each end of each sensor was devised. The four-sensor packages were arranged in a cardboard storage container shown in Figure 50 and Figure 51.

Figure 50. Array of Sensor Housings

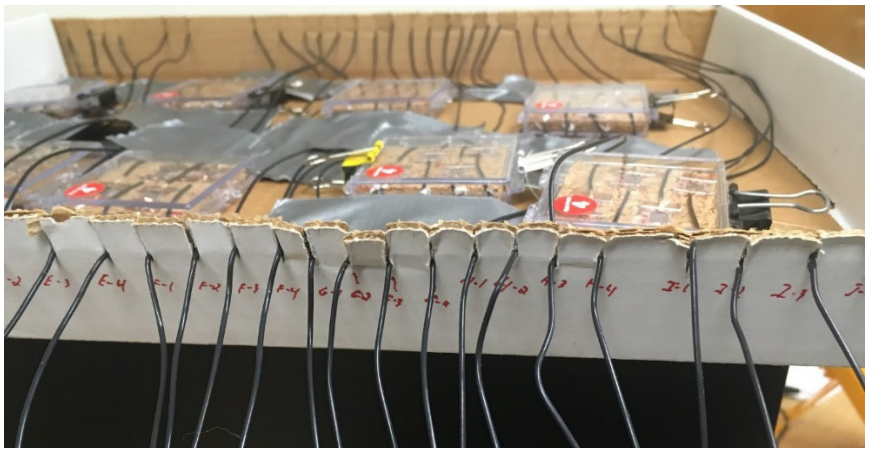

Figure 51. Method of Organization for Sensor Measurements

Since the most important result from Iteration 2 proved that the sensors were sensitive to light, the Iteration 3 sensors were fully shielded from all ambient light. After placing the chip housings in the top of the storage container, the rest of the cardboard container was set atop the sensor array in Figure 50. The final product is presented in Figure 52, showing it as it was irradiated by the PuBe source. In the figure, the sensor box is shown on top of high-density polyethylene, used to moderate neutrons from the PuBe source underneath. In the bottom left corner, a neutron detector from LLNL was used to measure the sensor's neutron fluence exposure.

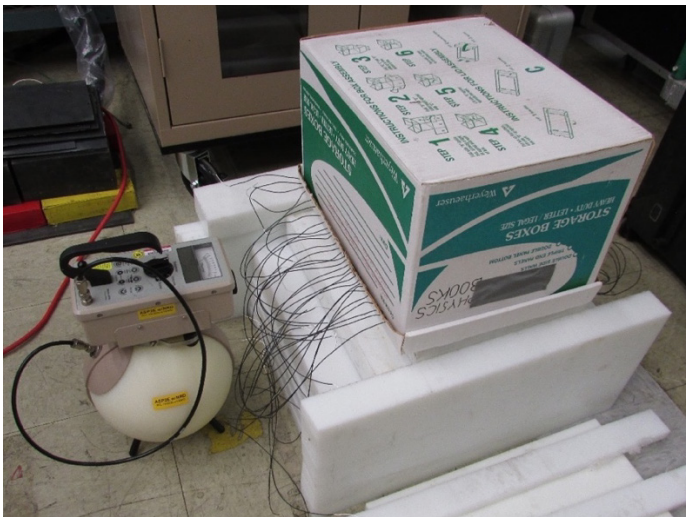

Figure 52. Shielded Sensors Exposed to PuBe Source

Using the processes discussed in Section II.B.2.c, where the products of the boron-10 (n,α) capture reaction break the underlying C-C bonds of the sensors, the expected results going into the experiment for each nanotube solution mixture follow.

- BNNT+CNT sensors: increase in resistance expected. The high-energy α and lithium particles should break the C-C bonds that form the electrical path across electrodes, leading to defects in the conduction path and increasing the resistance.

- BNNT only: no change or a resistance decrease expected. The BNNTs, as insulators, never formed a conductive path between electrodes before the experiment began. That was unlikely to change upon irradiation. But if enough created lithium ions were trapped in the BNNT structure to form a conductive link across electrodes, a possible decrease in resistance could be detected.

- CNT only: no change. CNTs are almost completely transparent to neutron radiation. Therefore, no change should be seen in the CNT only chips.

(1) Run 1: Ten Minute Exposures to PuBe Source

Run 1 exposed the sensor arrays in three ten-minute doses to the same PuBe source used in Iteration 2 using the set up shown in Figure 52. Only ten of the original 20 BNNT+CNT sensors were used in the experiment, as the remainder did not produce consistent measurements while determining their baseline to use as reliable sensors. After the first ten minutes, eight of the ten initially stable BNNT+CNT sensors' resistance increased, as expected. The BNNT-only sensors had resistance values too high to measure to start with and remained too high to measure after the first exposure. No change was detected in the CNT chips after the first exposure.

The measurements did not change after either of the subsequent two iterations of ten-minute exposures, which led to two conclusions. First, since throughout the 30 minutes, only the BNNT+CNT chips showed a definitive increase in resistance, and the CNT chips showed no change, the resistance change was very likely due to the neutron radiation.

Second, because no subsequent changes were detected in the second and third exposures, the sensor materials were likely saturated during the first exposure. Table 3 provides the resistance measurements throughout Iteration 3 for the eight chips with changing resistance. There is a clear resistance increase in the eight chips, while the other two stable chips (not included in the table), did not show any change.

Table 3 Resistance Measurements from Sensors for Iteration 3.

			Resistance Post-Exposure (Ohms)					
Chip Name	Average pre-radiation resistance (Ohms)	Standard deviation (Ohms)	0 minutes	10 minutes	20 minutes	30 minutes	30 minutes +10 Gamma	180 minutes rest
A1	39.50	0.15	39.7	40.3	40.3	40.3	40.3	40.2
B1	777.00	48.86	831	953	940	938	938	937
E1	415.00	12.36	434	443.5	443.6	444	444.5	443
F1	5064.50	651.30	4830	5483	5492	5495	5490	5456
F2	2857.30	233.94	3105	3483	3486	3485	3483	3463
G1	408.70	1.22	417	489.6	491	491	491	490
G2	1323.50	2.59	1315	2285	2289	2292	2292	2285
I1	1695.50	24.43	1739	2737	2739	2740	2744	2740

(2) Run 2: High-Energy Gamma Exposure

As noted in Equations 4 and 5, the three products from the decay of the boron-10 (n,α) capture reaction are a lithium ion, an α particle, and a high-energy gamma ray (~1MeV). In order to verify the prediction that the energetic lithium ions and α particles were the principle contributors of resistance increase via the destruction of C-C bonds, the sensors were exposed to a cobalt-60 gamma source for ten minutes. As shown in the cobalt decay process in Figure 3, the gamma rays produced from cobalt-60 are also ~1MeV, so it was a good source to test the prediction. If no change in resistance occurred, it would confirm that gamma radiation was not a large contributor to the changes in resistance seen in Run 1. Following the ten minutes of exposure, no changes were recorded in any of the sensors and the expectations were confirmed.

The final measurement was completed after the chips had not been exposed to light or any form of nuclear radiation for three hours. This measurement was taken to discover if the changes seen in Run 1 were permanent. Table 3 and Figure 53 both show that the change in resistance obtained after the first ten minutes remained constant even after the post-exposure three-hour rest period. Figure 53 shows an averaged and normalized graph

of the results from Table 3. The eight BNNT+CNT chips that increased in resistance generally grouped themselves into three categories, chips with resistance increases of ~68%, ~20%, and ~8%. The chips are shown with their respective groups in the figure, where the zero-minute mark is the normalized (to one) initial resistance of the chips. The purple line with triangle markers shows the response of the CNT only chips, displaying their lack of change throughout the entire experiment.

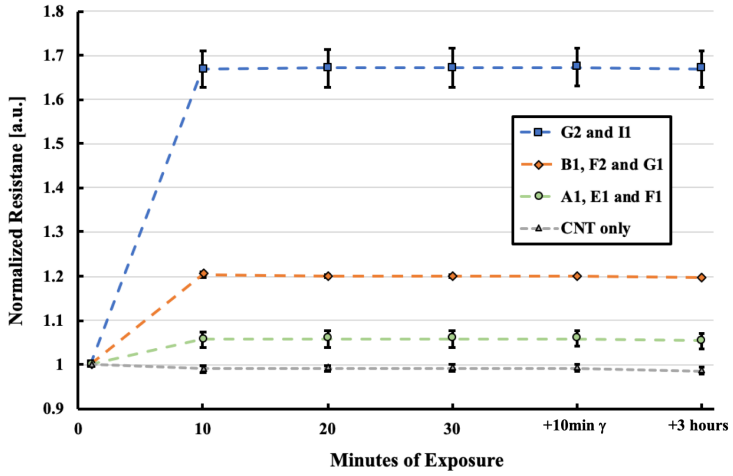

Figure 53. Iteration 3 Sensor Response

(3) Discussion of Iteration 3 Findings

As initially theorized, the boron-10 enriched BNNTs in combination with a CNT electrical substrate proved to be a feasible thermal neutron detector. By modifying the chips through two iterations of testing, analysis, and redesign, the final sensor design responded as expected to neutron irradiation. After exposure at LLNL, the increase in resistance of the eight chips shown in Figure 53 led to the successful conclusion of testing, and the planning of follow-on work, to be discussed in Chapter V.

THIS PAGE INTENTIONALLY LEFT BLANK

V. CONCLUSIONS AND FUTURE WORK

In order to create a functional radiation nose, identification and testing of materials used as receptors must first be completed. Through three iterations of designing, testing, and analysis of various sensors, this thesis proved that CNTs and BNNTs can be used as one of the receptors for the nose detector. Building upon this success and combining with other known detection materials can lead the way toward a new radiation detector applicable across many fields.

The capacitive sensor did not register radiation as expected, but areas for improvement were identified through its design, testing, and modeling process. This chapter will discuss conclusions and a way forward for the resistive detector followed by the capacitor detector and will end with a way forward for using the materials in a nose-style detector.

A. CONCLUSIONS FOR THE RESISTIVE NEUTRON SENSOR

This project confirmed the feasibility of a nanotube-based neutron detector. Through three iterations of design and testing the neutron detector, a successful sensor was created and accomplished the goal of registering the presence of thermal neutrons. By using an iterative approach and capitalizing on lessons learned from each iteration, an enriched boron-10 BNNT/CNT mixture on NASA interdigitated chips demonstrated a clear increase in resistance in response to thermal neutron irradiation.

The main lessons learned from the experiments involved the sensor design, the materials used, and the necessary use of environmental shielding. The first iteration narrowed down the general design of the chip from a possible 16-pad sensor to an interdigitated finger design. The 16-pad design limited the effective detection area of the sensor and, at that time, involved too much circuitry to create a simple, effective detector. The second iteration showed that natural boron BNNTs were not sufficient detectors and enriched boron-10 BNNTs were necessary for the sensors. It also showed that the NASA interdigitated chips provided more effective and stable measurements than the NPS chips. Most importantly, work from Iteration 2 specified the necessity of shielding the chips from

light exposure due to the semiconducting nature CNTs and their changing resistance in response to light. The gap between electrodes was bridged with a minimally thick layer of CNTs and enriched BNNTs in order to prevent a shielding effect where nuclear interactions only take place on the top layer, leaving the bottom layer, with the important electrical paths, unchanged.

B. FUTURE WORK FOR THE RESISTIVE NEUTRON SENSOR

The two major areas of future work for the neutron detector are more precise categorization of near real-time measurement and testing different moderating materials. The testing in Iteration 3 confirmed only that the response of the resistive sensors was saturated within the first ten minutes of exposure. Each boron-10 (n,α) capture reaction and subsequent emission of high-energy particles occurs in fractions of a second, so the detection of neutron radiation has the potential to be a very fast measurement. In order to categorize that response more accurately than achieved in prior work, the same sensors used in Iteration 3 should be used with real-time measurement tools. A characterization of source proximity and neutron fluence response could also be accomplished with the same sensor set up. This work could be completed with a combination of similar computer devices and software used in Iteration 1, with the stable chip design and housing used in Iteration 3.

Another area of future work could be the exploration of different moderating materials. It was difficult to specifically pin down the exact fluence of neutrons of a specific energy when using the PuBe source and layers of moderating polyethylene. Work to more precisely identify the exposure that was seen previously would be advantageous for future sensors. Following that work, the sensors should be exposed to the PuBe source using different moderating materials to change the energy spectrum which could categorize the effectiveness of the sensor across a wider range of neutron energies. This would allow for the characterization of response to neutron radiation at various energy levels. A final step in moderating materials would be the incorporation of the moderating materials into the chip itself. After identifying an effective amount of moderation material, polyethylene or

another, possibly denser, material could be incorporated into the housing of the chip itself, ensuring its portability and effectiveness.

C. CONCLUSIONS FOR THE CAPACITIVE SENSOR

Unfortunately, the capacitor sensor as designed and tested did not register any change in capacitance when exposed to gamma radiation. Two major reasons for the lack of response were likely the design of the chip and the use of PVA as its dielectric. The chip as designed had unstable and tall fingers for the electrodes, leading to possible unwanted connections between the electrodes. The electrodes were made very close together, which both added to the chances of unwanted connections, and limited the permeability of the PVA. The spacing may have been too close to allow the PVA to totally seep in and act as a full dielectric.

The chip layers consisted of Si on SiO_2 on Si, so the parasitic capacitance of the Si fingers and the Si substrate likely overwhelmed any change in capacitance between the electrodes themselves. COMSOL modeling shown and described in Section IV.B.3(1) confirmed that the electric field between the electrodes and substrate did indeed impact the capacitance measurements.

Finally, PVA itself may only be responsive as a detection material for high doses of gamma radiation. The goal of the capacitive sensor was to capture some of the more minor changes at low doses, but it was not able to do so.

D. FUTURE WORK FOR THE CAPACITIVE GAMMA SENSOR

In order to improve the capacitive sensor, two areas of future work should be attempted: a chip redesign, and an exploration of new materials as the dielectric. Major areas for redesign include the materials used for the fingers, their height, and the spacing between them. Instead of sandwiching an insulator between two semiconducting materials (Si-SiO_2-Si), future designs should layer materials similarly to the wafer fabrication described in Section III.B.2.a where a thin layer of metal was deposited on an insulator, sitting on a silicon substrate. That way, even though the electric field lines would still travel vertically through the insulator, more of the fringing fields could penetrate between the

fingers, in the presence of the dielectric. The fingers themselves should be shorter and spread further apart to ensure they are strong enough to withstand both probing and the fabrication process while leaving enough room for the dielectric material to fully occupy the vacant areas.

In order to test the redesign prior to fabrication, another model was created and run in COMSOL using some of the design modifications. That model is shown in Figure 54 with the shorter fingers and an etch all the way through the SiO_2. It pulled from the same dielectric values from Figure 11 to test the feasibility of the new design. Figure 55 shows the new theoretical capacitance values, which are similar to those determined for the original design. The modified design still provides a measurable capacitance reading and cause for testing it in future work.

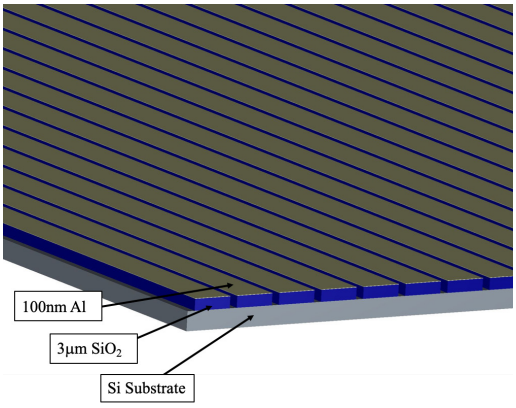

Figure 54. Proposed Design Change for Capacitor Chip

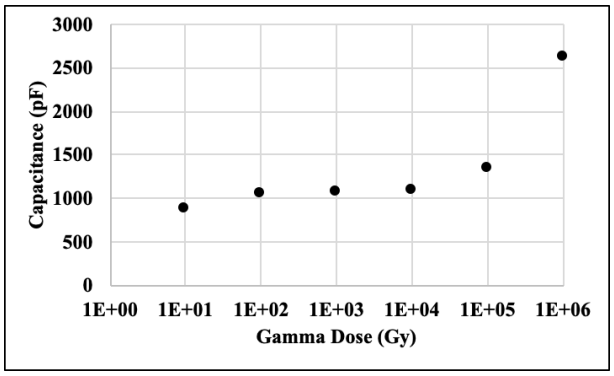

Figure 55. Theoretical Capacitance Values for Future Sensor

Replacing PVA as the dielectric material is another possible step for improvement of the sensor. In [45], Augustyniak et al. show that high-dose gamma detection is relevant and has its place in a wide-range radiation detector. However, for the purposes of initial detection, a more sensitive polymer should be used. In [46], Korostynska et al. use polyvinylidene fluoride doped with carbon at 4% or 6% by weight to respond to low doses of gamma irradiation. Future work should include alternative dielectrics, beginning possibly with polyvinylidene fluoride to take advantage of its similar properties to PVA and its sensitivity to low-dose gamma radiation.

E. FUTURE WORK TOWARD THE RADIATION ELECTRONIC NOSE

Ultimately, the success in neutron radiation detection and experience gained in gamma radiation detection demonstrated that a compound sensor could be formed and used for source identification. By combining detection materials, as discussed in Chapter I, a detector analogous in principle of operation as the human nose can be built. By expanding the receptors with further testing and identification of other effective materials, the combined detection of both gamma and neutron radiation could theoretically be used to identify fissile materials or other sources of radiation. The combination of these detection materials and computing power with the ability to recognize source spectra could feasibly lead to a full radiation nose. This process first requires the accurate characterization of each material's response to irradiation. Once characterized, the neutron and gamma source spectra of various sources could be programmed into the low cost processing unit, which would then compare a detection event to a library to determine the source.

This approach may not be limited to radiation sources. The nose concept could extend even farther by implementing toxic gas or biological agent detectors, forming even wider spectrum detectors for use in homeland defense, medicine, and space habitability. The key to this style of detector is accurately categorizing material responses, but in order to do that, effective materials must first be identified. This thesis proved that nanoscale, low-cost materials can be used as the beginning of that process and that many current detector technologies and materials should be seen as stepping stones toward more robust and compact detection capabilities.

THIS PAGE INTENTIONALLY LEFT BLANK

LIST OF REFERENCES

[1] P. W. Frame, "A history of radiation detection instrumentation," *Health Phys.*, vol. 88, no. 6, pp. 613–637, Jun. 2005. [Online]. Available: https://www.ncbi.nlm.nih.gov/pubmed/15891457

[2] Research and Markets, "Radiation Detection, Monitoring, & Safety Market by Product, Composition, Application - Global Forecast to 2022," I.D: 4539781, May 2018. [Online]. Available: https://www.researchandmarkets.com/research/ms9869/global_radiation?w=5

[3] K. Persaud and G. Dodd, "Analysis of discrimination mechanisms in the mammalian olfactory system using a model nose," *Nature*, vol. 299, no. 5881, pp. 352–355, Sep. 1982. [Online]. Available: https://www.ncbi.nlm.nih.gov/pubmed/7110356

[4] J. E. Dowling, *Understanding the brain: From cells to behavior to cognition*. New York, NY, USA: W.W. Norton & Company, 2018.

[5] D. Wilson, "How do we manage to remember smells despite the fact that each olfactory sensory neuron only survives for about 60 days and is then replaced by a new cell?" *Scientific American*. [Online]. Available: https://www.scientificamerican.com/article/experts-olfactory-neuron-turnover/

[6] A. D. Wilson and M. Baietto, "Applications and advances in electronic-nose technologies," *Sensors*, vol. 9, no. 7, pp. 5099–5148, 2009. [Online]. doi: 10.3390/s90705099

[7] K. Arshak, O. Korostynska, and C. Cunniffe, "Radiation nose concept," in *Proceedings of the 2006 IEEE Sensors Applications Symposium*, Houston, TX, USA, 2006. [Online]. doi: 10.1109/SAS.2006.1634232

[8] J. W. Han, M. Meyyappan, J. H. Ahn, and Y. K. Choi, "Liquid gate dielectric field effect transistor for a radiation nose," *Sens. Actuators Phys.*, vol. 182, pp. 1–5, Aug. 2012. [Online]. doi: 10.1016/j.sna.2012.05.038

[9] G. M. Gaukler, C. Li, Y. Ding, and S. S. Chirayath, "Detecting nuclear materials smuggling: Performance evaluation of container inspection policies," *Risk Anal. Off. Publ. Soc. Risk Anal.*, vol. 32, no. 3, pp. 531–554, Mar. 2012. [Online]. doi: 10.1111/j.1539-6924.2011.01696.x

[10] S. M. Brennan, A. M. Mielke, D. C. Tourney, and A. B. Maccabe, "Radiation detection with distributed sensor networks," *Computer*, vol. 37, no. 8, pp. 57–59, Aug. 2004. [Online]. doi: 10.1109/MC.2004.103

[11] Defense Advanced Research Projects Agency, “Radioactive Threat Detection System Completes Emergency Vehicle Test Deployment in Nation’s Capital,” March 1, 2017. [Online]. Available: https://www.darpa.mil/news-events/2017-03-01

[12] E. R. Benton and E. V. Benton, “Space radiation dosimetry in low-Earth orbit and beyond,” *Nucl. Instrum. Methods Phys. Res. Sect. B Beam Interact. Mater. At.*, vol. 184, no. 1–2, pp. 255–294, Sep. 2001. [Online]. doi: 10.1016/S0168-583X(01)00748-0

[13] C. Baldock *et al.*, “Polymer gel dosimetry,” *Phys. Med. Biol.*, vol. 55, no. 5, pp. R1-63, Mar. 2010. [Online]. doi: 10.1088/0031-9155/55/5/R01

[14] G. F. Knoll, *Radiation Detection and Measurement*, 3rd ed. New York, NY, USA: Wiley, 2000.

[15] Dosimetry Badge, “X-Ray monitoring badge,” *Dosimetry Badge*. Accessed April 15, 2019. [Online]. Available: https://www.dosimetrybadge.com/dosimeter-badge-cheap/

[16] A. L. Richards, “United States Customs and Border Protection’s radiation portal monitors at seaports,” Washington, DC, 2013.

[17] S. T. Thornton and A. F. Rex, *Modern Physics for Scientists and Engineers*. Fort Worth, TX, USA: Saunder’s College Pub, 1993.

[18] University of Virginia, “Pair production,” Accessed February 18, 2019. [Online]. Available: https://www.med-ed.virginia.edu/courses/rad/radbiol/01physics/phys-03-05.html

[19] W. E. Burcham, *Nuclear Physics: An Introduction*, 2d ed. London, UK: Longman, 1973.

[20] R. Rhodes, *The Making of the Atomic Bomb*. New York, NY, USA: Touchstone, 1988.

[21] n-Induced Cross Sections, “JANIS,” Accessed April 22, 2019. [Online]. Available: http://www.oecd-nea.org/janisweb/

[22] B. D. Milbrath, A. J. Peurrung, M. Bliss, and W. J. Weber, “Radiation detector materials: An overview,” *J. Mater. Res.*, vol. 23, no. 10, pp. 2561–2581, Oct. 2008. [Online]. doi: 10.1557/JMR.2008.0319

[23] D. J. Griffiths, *Introduction to Electrodynamics*, 4th ed. Boston, MA, USA: Pearson, 2013.

[24] C. R. Nave, “Polarization of dielectric,” *Hyperphysics.* Accessed April 2, 2019. [Online]. Available: http://hyperphysics.phy-astr.gsu.edu/hbase/electric/dielec.html.

[25] United States Nuclear Regulatory Commission, “High radiation doses,” October 2, 2017. [Online]. Available: https://www.nrc.gov/about-nrc/radiation/health-effects/high-rad-doses.html.

[26] Y. Watanabe, L. Warmington, and N. Gopishankar, “Three-dimensional radiation dosimetry using polymer gel and solid radiochromic polymer: From basics to clinical applications,” *World J. Radiol.*, vol. 9, no. 3, p. 112, 2017. [Online]. doi: 10.4329/wjr.v9.i3.112

[27] M. Hallensleben, R. Fuss, and F. Mummy, “Polyvinyl compounds, other,” in *Ullmann’s Polymers and Plastics: Products and Processes*, B. Elvers, Ed. Weinheim, Germany: Wiley-VCH Verlag GmbH & Co. KGaA, 2016, vol. 3 of 4, pp. 1141–1146.

[28] A. Shehap, R. A. Abd Allah, A. F. Basha, and F. H. Abd El-Kader, “Electrical properties of gamma-irradiated, pure, and nickel chloride-doped polyvinyl alcohol films,” *J. Appl. Polym. Sci.*, vol. 68, no. 5, pp. 687–698, May 1998. [Online]. doi: 10.1002/(SICI)1097-4628(19980502)68:5<687::AID-APP1>3.0.CO;2-K

[29] K. Prabha and H. S. Jayanna, “Influence of gamma irradiation on the dielectric properties of PVA-PS polymer blends,” *Int. J. Eng. Res. Appl.*, vol. 5, no. 8, pp. 05–09, Aug. 2015. [Online]: Available: http://www.ijera.com/papers/Vol5_issue8/Part%20-%204/B58040509.pdf

[30] F. H. Abd El-Kader, S. S. Hamza, and G. Attia, “Electrical and optical studies on gamma-irradiated pure and chromium-chloride-doped polyvinyl alcohol,” *J. Mater. Sci.*, vol. 28, no. 24, pp. 6719–6723, 1993. [Online]. doi: 10.1007/BF00356421

[31] N. M. El-Sawy, M. B. El-Arnaouty, and A. M. A. Ghaffar, “Gamma-irradiation effect on the non-cross-linked and cross-linked polyvinyl alcohol films,” *Polymer-Plastics Technol. Eng.*, vol. 49, no. 2, pp. 169–177, Jan. 2010. [Online]. doi: 10.1080/03602550903284248

[32] D. Sinha, “Structural modifications of gamma irradiated polymers: an FT-IR study,” *Adv. Appl. Sci. Res.*, vol. 3, no. 3, pp. 1365–1371, 2012. [Online]. Available: http://www.imedpub.com/articles/structural-modifications-of-gamma-irradiated-polymers-an-ftir-study.pdf

[33] E. A. Van Etten, E. S. Ximenes, L. T. Tarasconi, I. T. S. Garcia, M. M. C. Forte, and H. Boudinov, “Insulating characteristics of polyvinyl alcohol for integrated electronics,” *Thin Solid Films*, vol. 568, pp. 111–116, Oct. 2014. doi: 10.1016/j.tsf.2014.07.051

[34] T. Swu, C. A. Pongener, D. Sinha, and N. S. Sarma, “Effect of gamma radiation on dielectric properties of polyacetate polymer,” *Chem. Sin.*, vol. 4, no. 3, pp. 132–136, 2013. [Online]. Available: http://www.imedpub.com/articles/effect-of-gamma-radiation-on-dielectric-properties-of-polyacetate-polymer.pdf

[35] S. Iijima, “Helical microtubules of graphitic carbon,” *Nature*, vol. 354, no. 6348, pp. 56–58, Nov. 1991. [Online]. doi: 10.1038/354056a0

[36] M. Monthioux, “Introduction to carbon nanotubes,” in *Carbon Meta-Nanotubes: Synthesis, Properties, and Applications*, M. Monthioux, Ed. Chichester, West Sussex, U.K: Wiley-Blackwell, 2012, pp. 7–41.

[37] Y. Matsuda, J. Tahir-Kheli, and W. A. Goddard, “Definitive band gaps for single-wall carbon nanotubes,” *J. Phys. Chem. Lett.*, vol. 1, no. 9, pp. 2946–2950, Oct. 2010. [Online]. doi: 10.1021/jz100889u

[38] V. Zólyomi and J. Kürti, “First-principles calculations for the electronic band structures of small diameter single-wall carbon nanotubes,” *Phys. Rev. B*, vol. 70, no. 8, p. 085403, Aug. 2004. [Online]. doi: 10.1103/PhysRevB.70.085403

[39] B. Darwent, “Bond dissociation energies in simple molecules,” National Bureau of Standards, Washington, DC, USA, NSRDS-NBS 31, 1970. [Online]. Available: https://nvlpubs.nist.gov/nistpubs/Legacy/NSRDS/nbsnsrds31.pdf

[40] S. Munro. “SOI wafer notch reduction using the low frequency pulsing option on the STS ICP-RIE,” NanoFab, University of Alberta, 2009.

[41] G. Ciofani *et al.*, “A simple approach to covalent functionalization of boron nitride nanotubes,” *J. Colloid Interface Sci.*, vol. 374, no. 1, pp. 308–314, May 2012. [Online]. doi: 10.1016/j.jcis.2012.01.049

[42] R. Radev, “Neutron spectra fluence and dose rates from bare and moderated Cf-252 sources,” LLNL, Livermore, CA, USA, LLNL-TR-688699, 2016. [Online]. Available: https://e-reports-ext.llnl.gov/pdf/815667.pdf

[43] R. Radev and T. Mclean, “Neutron sources for standard-based testing,” LLNL, Livermore, CA, LLNL-TR-664160, 2014. [Online]. Available: https://e-reports-ext.llnl.gov/pdf/785407.pdf

[44] J. M. Xu, “Highly ordered carbon nanotube arrays and IR detection,” *Infrared Phys. Technol*., vol. 42, no. 3–5, pp. 485–491, Jun. 2001. [Online]. doi: 10.1016/S1350-4495(01)00102-5

[45] I. Augustyniak, J. Dziuban, P. Knapkiewicz, M. Matusiak, M. Olszacki, and P. Pons, “MEMS high-doses radiation sensor,” in *2013 Transducers & Eurosensors XXVII: The 17th International Conference on Solid-State Sensors, Actuators and Microsystems*, Barcelona, Spain, 2013. [Online]. doi: 10.1109/Transducers.2013.6627066

[46] O. Korostynska, K. Arshak, D. Morris, A. Arshak, and E. Jafer, “Radiation-induced changes in the electrical properties of carbon filled PVDF thick films,” *Mater. Sci. Eng. B*, vol. 141, no. 3, pp. 115–120, Aug. 2007. [Online]. doi: 10.1016/j.mseb.2007.06.025

THIS PAGE INTENTIONALLY LEFT BLANK

INITIAL DISTRIBUTION LIST

1. Defense Technical Information Center
   Ft. Belvoir, Virginia

2. Dudley Knox Library
   Naval Postgraduate School
   Monterey, California